CHAPTER 8

Carbon Cycle

Having completed our first grand tour of ocean biogeochemical cycles by reviewing and discussing the oceanic cycling of silicate, we are now ready to assess the marine carbon cycle, one of the most important and also most fascinating biogeochemical cycles in the ocean. In discussing this cycle, we will need to employ all the concepts that have been introduced and discussed in the previous chapters. In this chapter we will study how the marine carbon cycle works and how this cycle is connected with the atmospheric CO_2 concentration. We will see that the oceans contain approximately 60 times more carbon than the atmosphere and that the ocean therefore exerts a dominant control on atmospheric CO_2. We will introduce the concepts necessary to understand this fact and also discuss how biological and physical processes act together to reduce the surface concentration of inorganic carbon relative to the deep ocean. Without this reduction, atmospheric CO_2 would increase by more than 150 ppm, with the exact magnitude depending on the ocean carbon cycle model.

Our ability to understand and model the carbon cycle in the oceans has made large advances over the last twenty years since the Geochemical Ocean Section Study (GEOSECS) provided a first complete picture of the inorganic carbon distribution in the oceans. The recently completed Global Ocean CO_2 Survey, a joint effort between the Joint Global Ocean Flux Study (JGOFS) and the World Ocean Circulation Experiment (WOCE), provides us now with almost two orders of magnitude more data with improved precision and accuracy. Analysis and interpretation of this new data set has just begun, and it quite surely will provide us with many new insights on details of the marine carbon cycle. Over the last ten years, several global models of the carbon cycle in the oceans have been developed and successfully applied to many interesting questions. These models also increasingly incorporate the relevant processes prognostically, thus offering the opportunity to employ the models in conditions other than the current climate. However, there still exist large gaps in our understanding of several key issues.

Probably the largest puzzle in ocean carbon research is our inability to explain the large glacial-interglacial variations in atmospheric CO_2. As the oceans contain 60 times more carbon than the atmosphere and 17 times more carbon than is stored in the terrestrial biosphere (see figure 10.1.1), the causes for these variations must lie within the oceans. This lack of knowledge also hampers our ability to predict more reliably how the oceanic carbon cycle is going to change in the future as a result of human-induced climate change. The investigation of natural variability might offer some insight into how the marine carbon cycle responds to changes in the climatic state, but little is known regarding the role of the oceans on interannual to decadal timescales. While considerable advances have been made in pinning down the role of the oceans as a sink for anthropogenic CO_2, there still exists large uncertainties, especially regarding future uptake. We will deal with these outstanding issues in the last chapter of this book (chapter 10).

We start this chapter with an introduction that establishes a number of problems that provide a focal point for the discussion in the remainder of the chapter. We then construct the building blocks for answering most questions by introducing the inorganic carbon chemistry in seawater. Afterward we look at the processes that control surface ocean partial pressure of CO_2 and its seasonal variability. The last section extends the view into the water column by discussing the causes for the vertical variations of dissolved inorganic carbon and alkalinity.

8.1 Introduction

A major motivation to understand the ocean carbon cycle is its importance in controlling atmospheric CO_2, which, in turn, is an important factor of the climate system due its greenhouse gas properties (see chapter 10). How does the ocean exert this control? Are physical processes primarily responsible for controlling atmospheric CO_2, or does marine biology play the dominant role?

The first step to answering these questions is to look at the surface ocean distribution of pCO_2, because it is only the surface ocean that is in direct contact with the atmosphere and hence determines atmospheric pCO_2. Figure 8.1.1 shows a global map of the annual mean surface distribution of the sea-air difference in the partial pressure of CO_2 ($\Delta pCO_2 = pCO_2^{oc} - pCO_2^{atm}$; see also definition in equation (3.1.1)). The data show relatively wide bands of positive ΔpCO_2, i.e., supersaturated waters, in the tropical regions, with maximum values attained in the eastern equatorial Pacific and large bands of negative ΔpCO_2, i.e., undersaturated waters, in the mid-latitudes. The high latitudes in the south have near zero ΔpCO_2 values. The northern high latitudes exhibit a clear distinction between the North Pacific (positive ΔpCO_2) and the North Atlantic (negative ΔpCO_2). Since atmospheric CO_2 is relatively uniform over the globe, the variability in ΔpCO_2 is largely driven by variations in surface ocean pCO_2. What controls the distribution of surface ocean pCO_2?

As we will see in detail below, variations in surface ocean pCO_2 are determined by surface ocean temperature, salinity, dissolved inorganic carbon (*DIC*, the sum of all inorganic carbon species) and alkalinity (*Alk*, a measure of the excess of bases over acids). Variations in these properties, and hence pCO_2, stem from a complex interplay of chemical, biological, and physical processes. The transfer of CO_2 between the atmosphere and the surface ocean tends to eliminate any air-sea pCO_2 difference, but as we have seen at the end of chapter 3, it takes about 6 months to equilibrate a 40 m-thick surface layer with the atmosphere. This is long compared to the timescale of the biological and physical processes that tend to perturb the system. Why is the air-sea exchange of CO_2 so slow compared with other gases like oxygen or nitrogen? We have already briefly seen in chapter 3 that only about 1 out of 20 molecules that exchange with the atmosphere leads to a change in pCO_2. In order to fully understand this, we must first learn more about the reaction of CO_2 in seawater to

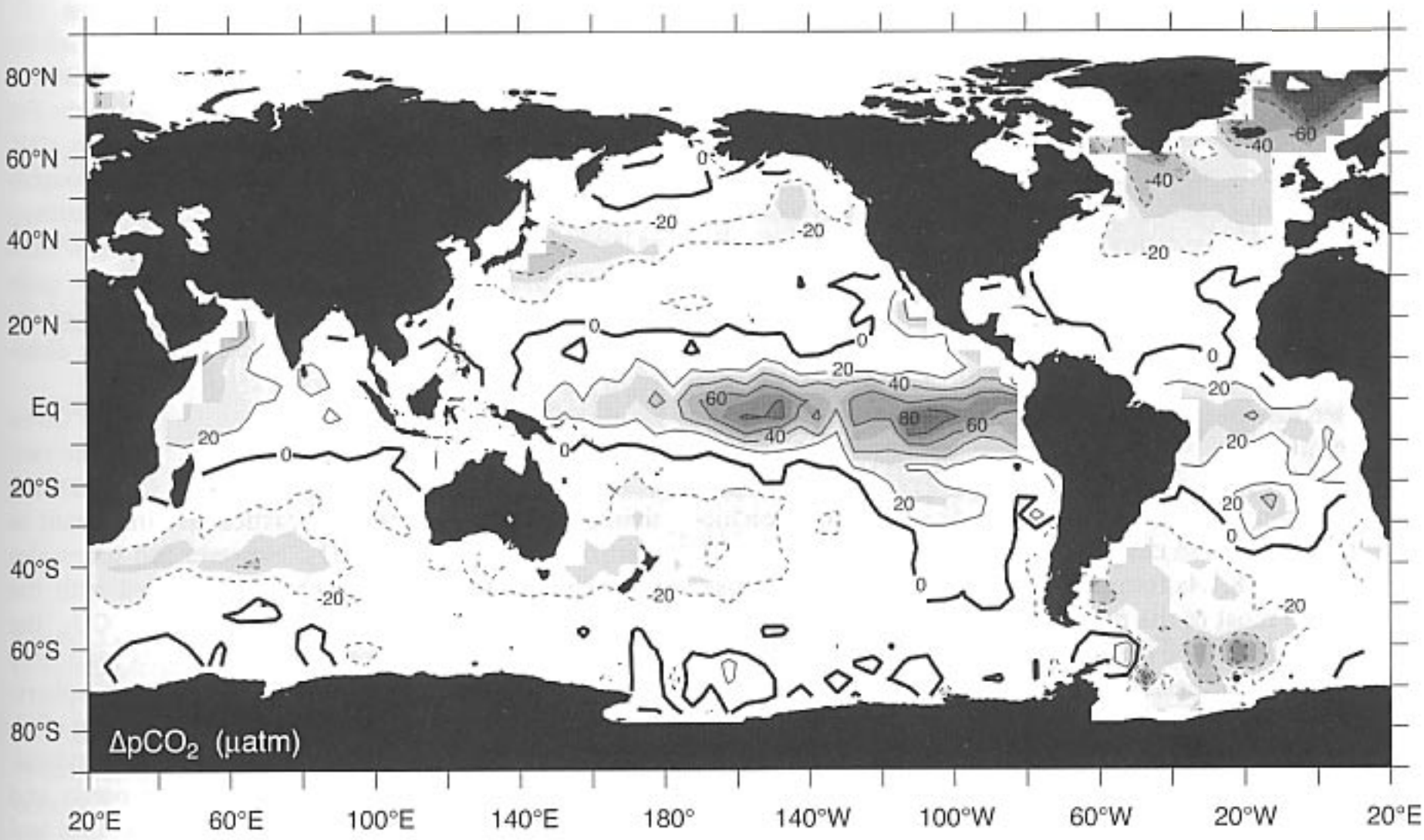

FIGURE 8.1.1: Map of the annual mean sea-air difference of the partial pressure of CO_2. See also color plate 3. Based on data from *Takahashi et al.* [2002].

form bicarbonate and carbonate ions. This topic will be covered in section 8.2. We will then investigate the controls on surface ocean pCO_2 in detail in section 8.3.

Although atmospheric CO_2 is controlled by surface ocean properties (i.e., temperature, salinity, *DIC*, and *Alk*), it is the deep ocean concentrations of *DIC* and *Alk* that ultimately determine the surface concentrations of these two chemicals and hence atmospheric CO_2. Figure 8.1.2 shows that the surface concentration of *DIC* is about 15% lower than deep ocean concentrations, while the gradient for *Alk* amounts to only about 5%. What are the mechanisms that maintain these gradients against the continuous action of ocean transport and mixing, which try to homogenize the ocean tracer distributions? Since these mechanisms operate against a gradient, they are often referred to as "pumps." The importance of these pumps becomes immediately clear when we turn them off and allow the ocean to homogenize completely (cf. also figure 4.1.3). The three-box model described in chapter 1 (figure 1.2.5) predicts that atmospheric CO_2 would rise from the preindustrial level of about 280 ppm to more than 420 ppm, i.e., an increase of about 50% [*Gruber and Sarmiento*, 2002]!

Given the importance of carbon for organisms, we expect that ocean biology constitutes such a pump. This would imply that *DIC* and *Alk* should have a distribution similar to phosphate. This indeed appears to be the case when we compare the sections of *DIC* and *Alk* (figures 8.1.3) with those of nitrate and phosphate (figure 5.1.2). Note that we normalized *DIC* and *Alk* here to constant salinity in order to remove variations due to the addition and removal of freshwater by precipitation and evaporation. We will be using the symbols *sDIC* and *sAlk* to distinguish these salinity-normalized concentrations (see detailed discussion in the next section below). Is biology the whole answer to our question of what causes the vertical *DIC* variations? If biological processes were the only ones affecting phosphate and *sDIC*, then all oceanic observations would lie on a single line on a plot of *sDIC* versus phosphate. This is because plants appear to take up CO_2 in a nearly constant ratio relative to phosphate (see discussion in panel 4.2.1). During respiration and remineralization processes, both carbon and phosphate are then returned in dissolved inorganic form to the seawater in the same ratios (see discussion on stoichiometric ratios in chapter 5).

Figure 8.1.4a reveals that this is only partially the case. While most of the points indeed lie clustered around a line with a slope predicted from the stoichiometric ratio of photosynthesis and remineralization, the data also exhibit substantial systematic offsets from such a trend. In general, the data lie below the biological trend line for low concentrations and lie above the trend line for high concentrations. Clearly, processes other than photosynthesis, respiration, and remineralization play a role in creating the variations seen in *sDIC*. As shown in the inset, these processes are air-sea gas exchange and the formation and dissolution of mineral calcium carbonate, which affect *sDIC* but do not change phosphate. For example, given the strong relationship between *sDIC* and temperature (figure 8.1.4b), which follows roughly an expected trend defined by the temperature sensitivity of the *DIC* concentration in equilibrium with a fixed atmospheric CO_2, variations in temperature quite clearly must play a role as well. Determination of the relative role of these processes in controlling the distribution of *DIC* will be covered in section 8.4.

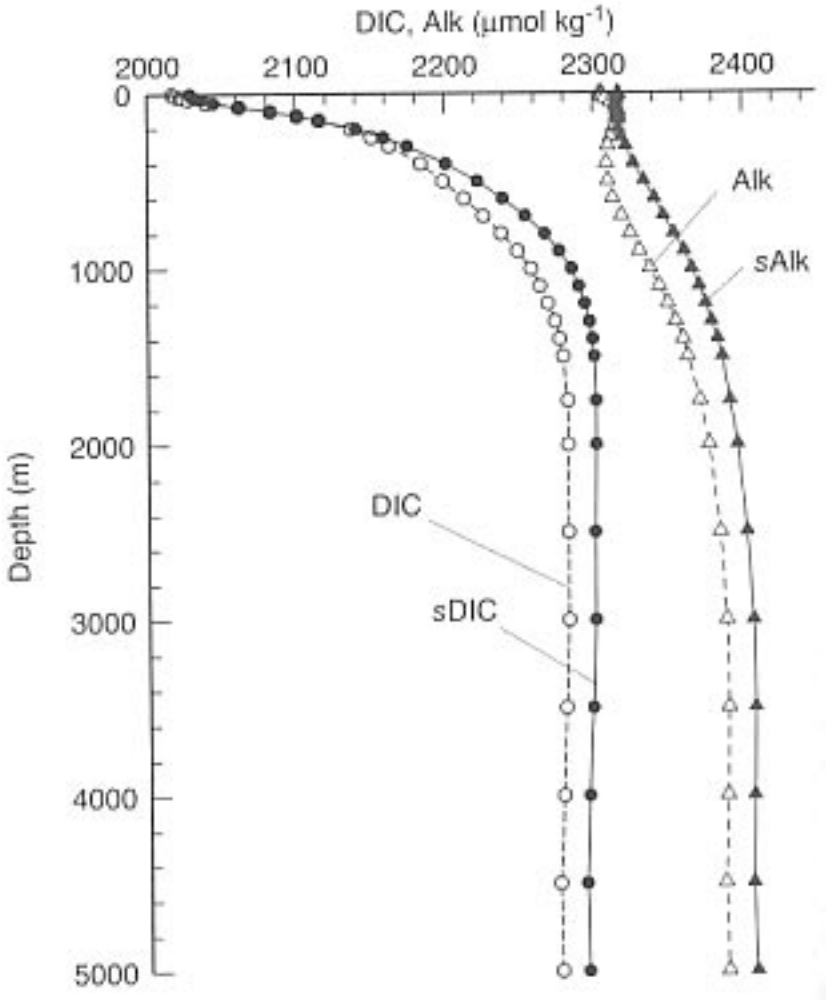

FIGURE 8.1.2: Horizontally averaged profiles of *DIC* and *Alk* in the global oceans. Also shown are the profiles of their salinity normalized concentrations, *sDIC*, and *sAlk*, computed by dividing the measured concentrations by the measured salinity and then multiplying the result with a standard salinity of 35. Based on the gridded climatological data from the GLODAP project [*Key et al.*, 2004].

What about the processes controlling alkalinity? Given the much smaller variations in *sAlk* relative to the variations in *sDIC* (figures 8.1.2 and 8.1.3), one might think that these processes are not particularly important in controlling atmospheric CO_2. However, on timescales of millenia and longer, such as associated with the glacial-interglacial changes in atmospheric CO_2, the cycling of alkalinity within the ocean and its sediments emerges as a key component controlling atmospheric CO_2. The main processes controlling the cycling of alkalinity are the biological production of mineral calcium carbonates ($CaCO_3$) in the surface ocean and dissolution of these minerals in the water column and in the sediments. We will introduce the basic chemistry of these reactions in this chapter, but discuss the

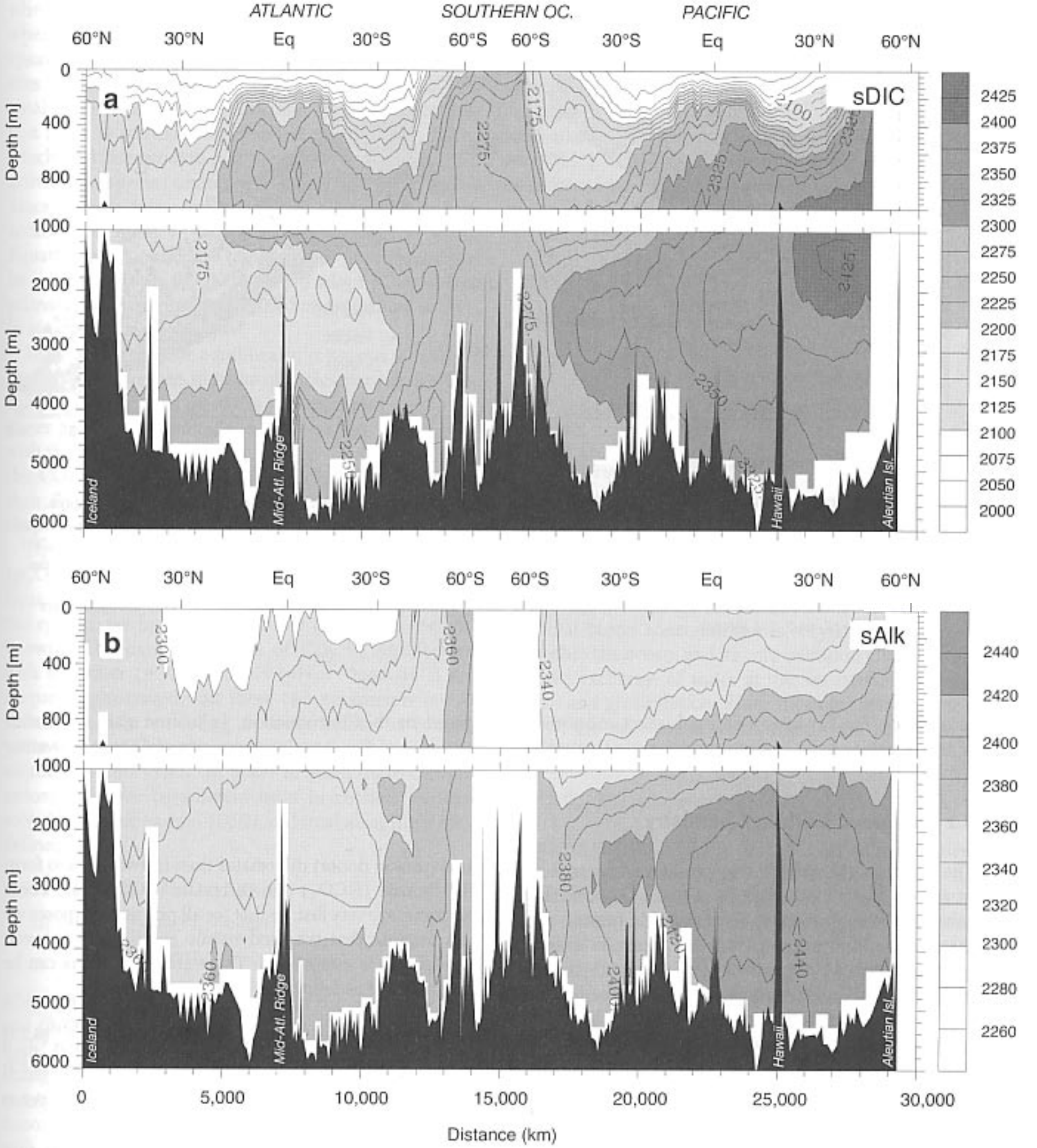

FIGURE 8.1.3: Vertical sections of salinity-normalized inorganic carbon system properties along the track shown in figure 2.3.3a. (a) Salinity-normalized *DIC* ($\mu mol\,kg^{-1}$). (b) Salinity-normalized *Alk* ($\mu mol\,kg^{-1}$). See also color plate 8.

cycling of $CaCO_3$ in chapter 9. The interaction of the oceanic $CaCO_3$ cycle with climate is taken up in chapter 10.

There is much about the ocean carbon cycle that is puzzling and sometimes even counterintuitive. For example, it is not self-evident why the ocean contains 98% and the atmosphere only 2% of the carbon stored in the combined reservoirs. For most other gases, like oxygen or nitrogen, this distribution pattern is actually reversed, despite the fact that all these gases have similar

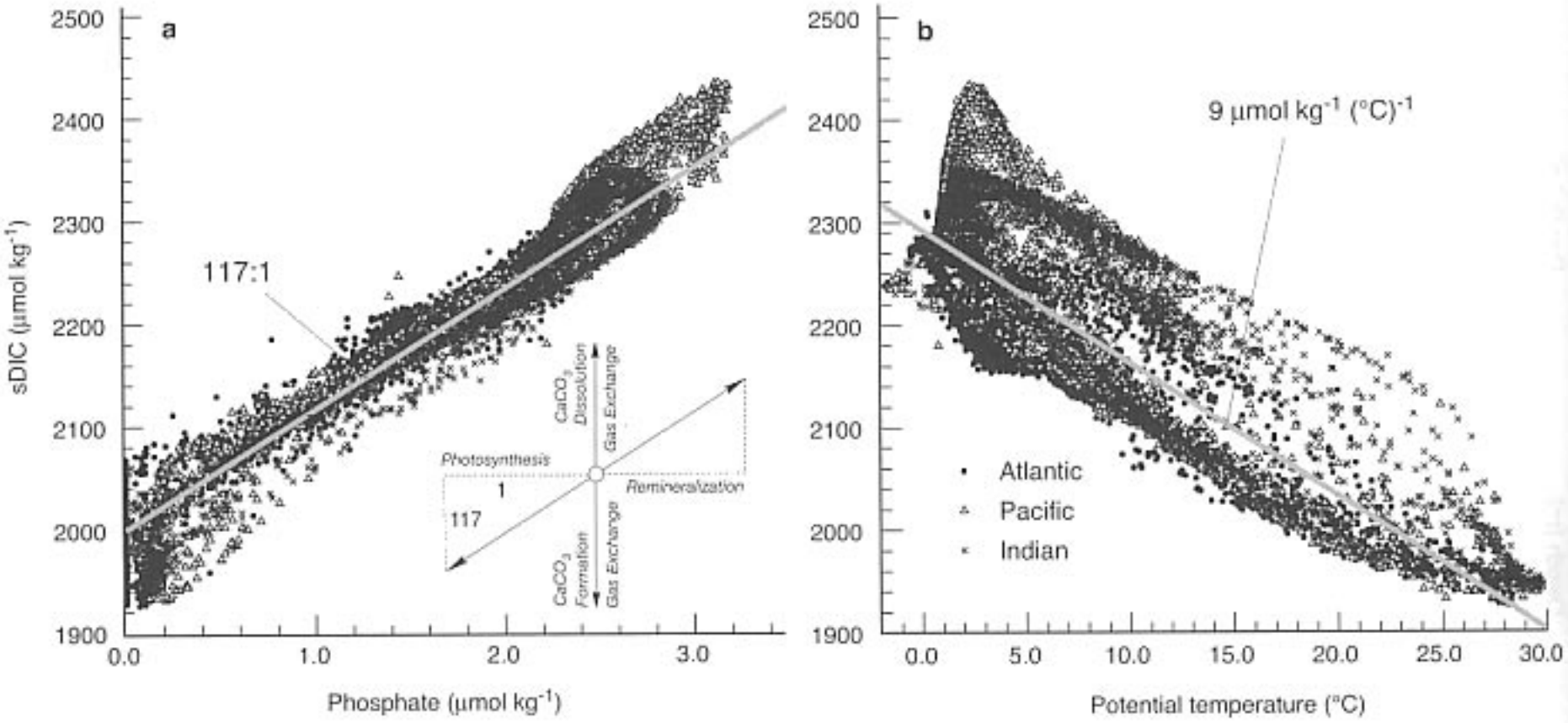

FIGURE 8.1.4: Plot of dissolved inorganic carbon, *DIC*, versus (a) phosphate and (b) potential temperature, using data from all depths. Both *DIC* and phosphate have been normalized to a constant salinity of 35, in order to remove the effects of evaporation and precipitation. The line in (a) shows the expected trend if all variations of *sDIC* were caused by biological processes. The inset shows the trends in *sDIC* and phosphate caused by photosynthesis, respiration, and remineralization, as well as the trends caused by air-sea gas exchange and the formation and dissolution of $CaCO_3$. The line in (b) shows the expected trend if all variations of *sDIC* were a result of differences in temperature. At constant oceanic pCO_2 and alkalinity, this trend is nearly 9 μmol kg^{-1} per degree Celsius [*Gruber et al.*, 1996]. Data are from WOCE legs A16, P16, and I9NI8S.

solubilities. The key to explaining this fact and almost all of the puzzles of the marine carbon cycle that we have posed in this introduction, is to first gain an understanding of the complex chemistry of CO_2 in seawater.

8.2 Inorganic Carbon Chemistry

The solution chemistry of carbon dioxide sets it apart from that of most other gases in that CO_2 not only dissolves in seawater but also acts as an acid (proton donor) that reacts with water to form free protons (H^+), and the conjugate bases bicarbonate (HCO_3^-) and carbonate (CO_3^{2-}). In this section we will introduce the basic concepts of these reactions and how they can be quantitatively described. We also attempt to establish some simple tools to aid in understanding the nonlinearities of the oceanic CO_2 system. For the purpose of this presentation we will employ a number of simplifications. The reader interested in a more thorough discussion is referred to *Dickson and Goyet* [1994].

When gaseous CO_2 dissolves in seawater, it first gets hydrated to form aqueous CO_2 ($CO_{2\,(aq)}$), which reacts with water to form carbonic acid (H_2CO_3). It is difficult to distinguish analytically between the two species $CO_{2(aq)}$ and H_2CO_3. As a result, it is usual to combine these two species and express the sum as the concentration of a hypothetical species, $H_2CO_3^*$ [*Stumm and Morgan*, 1981; *Dickson and Goyet*, 1994]. This hypothetical acid (proton donor) dissociates then in two steps to form bicarbonate (HCO_3^-) and carbonate (CO_3^{2-}) ions. These reactions are very fast, so that for all practical purposes we can assume that thermodynamic equilibrium between the species is established. These three reactions can be summarized as follows:

$$CO_{2\,(gas)} + H_2O \rightleftharpoons H_2CO_3^* \tag{8.2.1}$$

$$H_2CO_3^* \rightleftharpoons H^+ + HCO_3^- \tag{8.2.2}$$

$$HCO_3^- \rightleftharpoons H^+ + CO_3^{2-} \tag{8.2.3}$$

The equilibrium relationships between these species are given by

$$K_0 = \frac{[H_2CO_3^*]}{pCO_2} \tag{8.2.4}$$

$$K_1 = \frac{[H^+][HCO_3^-]}{[H_2CO_3^*]} \tag{8.2.5}$$

$$K_2 = \frac{[H^+][CO_3^{2-}]}{[HCO_3^-]} \tag{8.2.6}$$

where pCO_2 is the partial pressure of CO_2 in the air and where the brackets denote total concentrations. Strictly speaking, these equations should be expressed as activities rather than concentrations, but we neglect this small difference here. In particular, the CO_2 concentration in air is sometimes expressed as a fugacity, fCO_2, which is a thermodynamic property analogous to the activity of a species dissolved in water (see panel 3.2.1). Since fugacity takes the nonideality of CO_2 in air into account, its value is somewhat lower than the pCO_2. Equation (2) in panel 3.2.1 shows how the fugacity can be calculated from pCO_2. Here, we adopt pCO_2 as our primary quantity expressing the concentration of CO_2 in air.

In the literature, the equilibrium constants K_1 and K_2 are usually expressed in units of moles per kilogram of solution rather than in units of milimoles per cubic meter as adopted generally in this text. For consistency with the published literature, we use the symbol K_0 for the CO_2 solubility in units of $\mathrm{mol\,kg^{-1}\,atm^{-1}}$, rather than S_{CO_2}, which is in units of $\mathrm{mmol\,m^{-3}\,atm^{-1}}$ (see chapter 3).

The CO_2 system so far consists of 5 unknowns (pCO_2, $[H_2CO_3^*]$, $[HCO_3^-]$, $[CO_3^{2-}]$, and $[H^+]$) and 3 equations (8.2.4, 8.2.5, and 8.2.6). In order to determine the system, we have to specify any two of the five unknowns. The partial pressure of CO_2 in equilibrium with the water (pCO_2) and pH ($\mathrm{pH} = -\log_{10}[H^+]$) are frequently measured, but these two parameters are ill suited to use in modeling, because neither is conservative with respect to changes in state (i.e., temperature, salinity, and pressure). In order to avoid these complications, the two parameters used in models are dissolved inorganic carbon (*DIC*) and total alkalinity (*Alk*), defined as

$$DIC = [H_2CO_3^*] + [HCO_3^-] + [CO_3^{2-}] \tag{8.2.7}$$

$$Alk = [HCO_3^-] + 2[CO_3^{2-}] + [OH^-] - [H^+] + [B(OH)_4^-] + \text{minor bases} \tag{8.2.8}$$

where $[OH^-]$ is the concentration of the hydroxide ion, and $[B(OH)_4^-]$ is the concentration of the borate ion. Both *DIC* and *Alk* are conservative with respect to changes in state. The total alkalinity is a measure of the excess of bases (proton acceptors) over acids (proton donors), and is operationally defined by the titration with H^+ of all weak bases present in the solution (see *Dickson* [1981] for an exact definition of alkalinity). Alternatively, total alkalinity can be viewed as the charge balance of all strong acids and bases unaffected by this titration, i.e.,

$$Alk = [Na^+] + [K^+] + 2[Mg^{2+}] + 2[Ca^{2+}] + \text{minor cations} - [Cl^-] - 2[SO_4^{2-}] - [Br^-] - [NO_3^-] - \text{minor anions} \tag{8.2.9}$$

The contribution of the minor bases like phosphate, silicate, and sulphate to variations in *Alk* are usually well below one percent, and we are therefore going to neglect them.

The definition of dissolved inorganic carbon and total alkalinity introduces four new unknowns (DIC, *Alk*, $[OH^-]$, $[B(OH)_4^-]$) for a total of 9, but only two new equations for a total of 5. Additional constraints on the system of equations are needed. The hydroxide ion originates from the self-dissociation of water

$$H_2O \rightleftharpoons H^+ + OH^- \tag{8.2.10}$$

with the dissociation constant

$$K_w = [H^+][OH^-] \tag{8.2.11}$$

Borate is formed by the dissociation of boric acid by the reaction

$$H_3BO_3 + H_2O \rightleftharpoons H^+ + B(OH)_4^- \tag{8.2.12}$$

with the dissociation constant

$$K_B = \frac{[H^+][B(OH)_4^-]}{[H_3BO_3]} \tag{8.2.13}$$

The total boron concentration is very nearly conservative within the ocean, and its concentration changes only with net exchange of water at the sea surface by evaporation and precipitation. Since these processes control salinity, the total boron concentration can be assumed to be proportional to the salinity, *S*,

$$[B(OH)_4^-] + [H_3BO_3] = c \cdot S \tag{8.2.14}$$

Equations (8.2.11), (8.2.13), and (8.2.14) add three new equations and 1 new unknown, H_3BO_3. We therefore end up with 8 equations and 10 unknowns (see table 8.2.1). As was the case above, the specification of two unknowns completely determines the inorganic carbon system. Models commonly employ *DIC* and *Alk* as state variables of the carbon system, whereas at sea, often a combination of pCO_2, *DIC*, and *Alk* are measured. With the introduction of a method for the high-precision determination of pH [*Clayton and Byrne*, 1993], this quantity is being increasingly determined as well. This system of eight equations cannot be solved analytically, because a higher order polynomial equation has to be solved. Iterative methods are commonly used (see table 8.2.1).

Table 8.2.2 lists the empirical equations for calculating the dissociation constants. Note that these constants are given in units of moles per kilogram of solution. The exact values for the dissociation constants, K_1 and K_2, of carbonic acid and bicarbonate, respectively, are currently still subject to considerable debate [*Millero et al.*, 1993; *Lee and Millero*, 1995; *Lee et al.*, 1997; *Lueker*, 1998]. We have adopted here the dissociation constants of *Mehrbach et al.*

Unknowns:

$$CO_{2[gas]},\ H_2CO_3^*,\ HCO_3^-,\ CO_3^{2-},\ H^+,\ OH^-,\ B(OH)_4^-,\ H_3BO_3,\ DIC,\ Alk$$

Reactions:

$$CO_{2[gas]} + H_2O \overset{K_0}{\rightleftharpoons} H_2CO_3^* \tag{1}$$

$$H_2CO_3^* \overset{K_1}{\rightleftharpoons} H^+ + HCO_3^- \tag{2}$$

$$HCO_3^- \overset{K_2}{\rightleftharpoons} H^+ + CO_3^{2-} \tag{3}$$

$$H_2O \overset{K_w}{\rightleftharpoons} H^+ + OH^- \tag{4}$$

$$H_3BO_3 + H_2O \overset{K_B}{\rightleftharpoons} H^+ + B(OH)_4^- \tag{5}$$

Equilibrium constants:

$$K_0 = \frac{[H_2CO_3^*]}{pCO_2} \tag{6}$$

$$K_1 = \frac{[H^+][HCO_3^-]}{[H_2CO_3^*]} \tag{7}$$

$$K_2 = \frac{[H^+][CO_3^{2-}]}{[HCO_3^-]} \tag{8}$$

$$K_w = [H^+][OH^-] \tag{9}$$

$$K_B = \frac{[H^+][B(OH)_4^-]}{[H_3BO_3]} \tag{10}$$

Concentration definitions[1]*:*

$$DIC = [H_2CO_3^*] + [HCO_3^-] + [CO_3^{2-}] \tag{11}$$

$$Alk = [HCO_3^-] + 2[CO_3^{2-}] + [OH^-] - [H^+] + [B(OH)_4^-] \tag{12}$$

$$TB = [B(OH)_4^-] + [H_3BO_3] = c \cdot S \tag{13}$$

Solution:
In models of the ocean carbon cycle, two cases are most commonly encountered: (a) specifying *DIC* and *Alk* and calculating pCO_2; (b) specifying pCO_2 and *Alk* and computing *DIC*.

(a) *DIC* and *Alk*:
The goal is to rewrite the equation for *Alk* (12) in terms of the known parameters *DIC* and *TB*, and then solve the resulting equation for unknown $[H^+]$. As a first step, we use (7), (8), and the *DIC* definition (11) to write expressions for $[HCO_3^-]$ and $[CO_3^{2-}]$ that contain only $[H^+]$ as an unknown. In the case of $[HCO_3^-]$, this is done as follows. Solve (7) for $[H_2CO_3^*]$ and insert into (11). Similarly, solve (8) for $[CO_3^{2-}]$ and insert into (11). This gives

$$DIC = \frac{[H^+][HCO_3^-]}{K_1} + [HCO_3^-] + \frac{K_2[HCO_3^-]}{[H^+]} \tag{14}$$

Next, we use (8), solve it for $[HCO_3^-]$, and insert it into (14). This gives a second equation for *DIC*:

$$DIC = \frac{[H^+]^2[CO_3^{2-}]}{K_1 K_2} + \frac{[H^+][CO_3^{2-}]}{K_2} + [CO_3^{2-}] \tag{15}$$

Solving (14) for $[HCO_3^-]$ and (15) for $[CO_3^{2-}]$, respectively, and inserting the results into (12) eliminates $[CO_3^{2-}]$ and $[HCO_3^-]$ from this latter equation. The concentrations of $[OH^-]$ and $[B(OH)_4^-]$ are similarly eliminated using (9), (10), and (13). This results in our final equation, which is fourth order in the unknown $[H^+]$. This equation can then be solved for $[H^+]$ using an iterative approach. Once $[H^+]$ has been calculated, pCO_2 can be calculated from

$$pCO_2 = \frac{[DIC]}{K_0} \frac{[H^+]^2}{[H^+]^2 + K_1[H^+] + K_1 K_2} \tag{16}$$

where this equation has been derived by solving (6) for pCO_2, and then using (7), (8), and (11) to eliminate the unknowns $[H_2CO_3^*]$, $[HCO_3^-]$, and $[CO_3^{2-}]$. See also (17)–(19) below.

(b) *Alk* and pCO_2:
Rewrite the equations for the three carbon species, i.e., (6), (7), and (8), in terms of $[H^+]$ and pCO_2, thus

$$[H_2CO_3^*] = K_0\, pCO_2 \tag{17}$$

$$[HCO_3^-] = \frac{K_0\, K_1\, pCO_2}{[H^+]} \tag{18}$$

$$[CO_3^{2-}] = \frac{K_0\, K_1\, K_2\, pCO_2}{[H^+]^2} \tag{19}$$

Substitute these terms into the equation for *Alk* (12) and also recast the other species, i.e., $[OH^-]$ and $[B(OH)_4^-]$, in terms of $[H^+]$ and total concentrations. The resulting equation can again be solved using an iterative approach. Once $[H^+]$ is found, *DIC* is calculated using (11) and (17)–(19).

[1] The minor contributions of other weak bases to alkalinity are neglected here (see Dickson and Goyet [1994] for more details).

TABLE 8.2.2
Equations used to calculate seawater equilibrium constants
T: Temperatures in [K], S: Salinity on the practical salinity scale.

Equation		*Source*
Solubility of CO_2 ($mol\,kg^{-1}\,atm^{-1}$):		
$\ln K_0 = -60.2409 + 93.4517\left(\frac{100}{T}\right) + 23.3585\ln\left(\frac{T}{100}\right) + S\left(0.023517 - 0.023656\left(\frac{T}{100}\right) + 0.0047036\left(\frac{T}{100}\right)^2\right)$	(20)	[*Weiss*, 1974]
Dissociation constants of CO_2† ($mol\,kg^{-1}$):		
$-\log K_1 = -62.008 + \frac{3670.7}{T} + 9.7944\ln(T) - 0.0118\,S + 0.000116\,S^2$	(21)	[*Mehrbach et al.*, 1973] as refitted by *Dickson and Millero* [1987]
$-\log K_2 = +4.777 + \frac{1394.7}{T} - 0.0184\,S + 0.000118\,S^2$	(22)	[*Mehrbach et al.*, 1973] as refitted by *Dickson and Millero* [1987]
Dissociation constants of other species† [$(mol\,kg^{-1})^2$] for K_w and ($mol\,kg^{-1}$) for K_b:		
$\ln K_w = 148.96502 + \frac{-13847.26}{T} - 23.6521\ln(T) + S^{\frac{1}{2}}\left(-5.977 + \frac{118.67}{T} + 1.0495\ln(T)\right) - 0.01615\,S$	(23)	[*Millero*, 1995]
$\ln K_b = \frac{1}{T}(-8966.9 - 2890.53\,S^{0.5} - 77.942\,S + 1.728\,S^{1.5} - 0.0996\,S^2) + 148.0248 + 137.1942\,S^{0.5} + 1.62142\,S + 0.053105\,S^{0.5}\,T + \ln(T)\,(-24.4344 - 25.085\,S^{0.5} - 0.2474\,S)$	(24)	[*Dickson*, 1990]
Total boron equation ($\mu mol\,kg^{-1}$):		
$TB = 11.88 \cdot S$	(25)	[*Uppström*, 1974]

† All dissociation constants are given with respect to the seawater pH scale [*Dickson*, 1993].

[1973] as refitted by *Dickson and Millero* [1987] because they appear to produce internally consistent data when considering *DIC*, *Alk*, and pCO_2, as is typically the case in models [*Lee et al.*, 1997; *Lueker*, 1998; *Wanninkhof et al.*, 1999b; *Lueker et al.*, 2000]. However, the refitted dissociation constants of *Mehrbach et al.* [1973] appear to be problematic when pH or other parameters of the CO_2 system are considered [*Lee et al.*, 1997]. Typical values for the dissociation constants and the solubility at various temperatures are listed in table 8.2.3.

Solving the equations for global mean surface seawater properties yields

$$\begin{aligned} DIC &= [H_2CO_3^*] + [HCO_3^-] + [CO_3^{2-}] \\ &= \quad 0.5\% \quad 88.6\% \quad 10.9\% \\ Alk &= [HCO_3^-] + 2[CO_3^{2-}] + [OH^-] - [H^+] + [B(OH)_4^-] \\ &= 76.8\% \quad 18.8\% \quad 0.2\% \quad 4.2\% \end{aligned}$$

(see also table 8.2.4). This shows that only a very small fraction of the dissolved inorganic carbon exists as dissolved CO_2, and that the majority of the carbon exists as bicarbonate ion and a smaller amount in the form of carbonate ion. Therefore, for many purposes, we can approximate *DIC* as the sum of bicarbonate and carbonate ions only:

$$DIC \approx [HCO_3^-] + [CO_3^{2-}] \tag{8.2.15}$$

This computation also reveals that the contribution of the dissociation of water to variations in alkalinity is negligible and that the contribution of borate is of the order of a few percent. Therefore, *Alk* can often be reasonably well approximated by the carbonate alkalinity, i.e.,

$$Alk \approx Carb\text{-}Alk = [HCO_3^-] + 2[CO_3^{2-}] \tag{8.2.16}$$

TABLE 8.2.3
Numerical values of the equilibrium constants as a function of temperature for a salinity of 35

Temp. °C	$-\log_{10} K_0$ *mol kg*$^{-1}$ *atm*$^{-1}$	$-\log_{10} K_1$ *mol kg*$^{-1}$	$-\log_{10} K_2$ *mol kg*$^{-1}$	$-\log_{10} K_w$ *mol kg*$^{-1}$	$-\log_{10} K_b$ (*mol kg*$^{-1}$)^2	$-\log_{10} \frac{K_2}{K_1}$	$-\log_{10} \frac{K_2}{K_0 K_1}$ *kg mol*$^{-1}$ *atm*
0	1.202	6.106	9.384	14.300	8.906	3.277	2.076
2	1.235	6.080	9.346	14.203	8.878	3.266	2.031
4	1.267	6.055	9.310	14.108	8.851	3.255	1.988
6	1.298	6.030	9.274	14.015	8.824	3.244	1.945
8	1.329	6.007	9.238	13.924	8.797	3.232	1.903
10	1.358	5.984	9.203	13.834	8.771	3.219	1.862
12	1.386	5.962	9.169	13.746	8.746	3.207	1.821
14	1.413	5.941	9.135	13.659	8.721	3.194	1.781
16	1.439	5.920	9.101	13.575	8.696	3.181	1.741
18	1.465	5.901	9.068	13.491	8.671	3.167	1.702
20	1.489	5.882	9.035	13.409	8.647	3.154	1.664
22	1.513	5.863	9.003	13.329	8.623	3.140	1.627
24	1.536	5.846	8.971	13.250	8.600	3.125	1.590
26	1.558	5.829	8.940	13.172	8.576	3.111	1.553
28	1.579	5.813	8.909	13.096	8.553	3.096	1.517
30	1.599	5.797	8.878	13.021	8.530	3.081	1.482

All dissociation constants are given with respect to the seawater pH scale [*Dickson*, 1993]. Sources: K_0: *Weiss* [1974]; K_1 and K_2: *Mehrbach et al.* [1973] as refitted by *Dickson and Millero* [1987]; K_b: *Dickson* [1990]; K_w: *Millero* [1995].

TABLE 8.2.4
Mean values of potential temperature, salinity, *sDIC*, *sAlk*, $H_2CO_3^*$, HCO_3^-, and CO_3^{2-} in the world oceans, based on data collected during the World Ocean Circulation Experiment

Region	θ °C	S	*sDIC* *μmol kg*$^{-1}$	*sAlk* *μmol kg*$^{-1}$	$[H_2CO_3^*]$ *μmol kg*$^{-1}$	$[HCO_3^-]$ *μmol kg*$^{-1}$	$[CO_3^{2-}]$ *μmol kg*$^{-1}$
Surface Ocean (0–50 m)							
Low and mid-lat.†	23.0	35.15	2003	2315	10	1772	221
Southern hemisphere high latitudes†	3.7	34.05	2119	2291	17	1977	125
Northern hemisphere high latitudes†	4.7	32.90	2049	2257	13	1889	147
Mean surface ocean	18.1	34.75	2026	2308	11	1815	200
Deep (>1200 m) and entire ocean							
Mean deep ocean	1.8	34.73	2280	2381	29	2164	86
Mean global ocean	3.6	34.73	2256	2364	28	2138	90

The carbon species have been calculated using the dissociation constants of *Mehrbach et al.* [1973] as given by *Dickson and Millero* [1987].
† Low and mid-latitudes: 45°S–45°N; High latitudes: south 45°S for the southern hemisphere, and 45°N–80°N for the northern hemisphere.

Combining these two equations ((8.2.15) and (8.2.16)) allows us to express the concentration of bicarbonate and carbonate in terms of *DIC* and *Alk* only:

$$[HCO_3^-] \approx 2 \cdot DIC - Alk \tag{8.2.17}$$

$$[CO_3^{2-}] \approx Alk - DIC \tag{8.2.18}$$

These two approximations are usually good to within about 10%. As we will see below, these approximation will provide a powerful tool for discussing many peculiarities of the CO_2 system in seawater.

In many studies, pH is used as a master variable. It is therefore instructive to investigate the inorganic carbon system in seawater also as a function of this parameter. Figure 8.2.1 shows how the concentration of the three inorganic carbon species varies as a function of pH for fixed *DIC*. Below $pK_1 = -\log K_1$, $H_2CO_3^*$ dominates. At $pH = pK_1$, $[H_2CO_3^*]$ is equal to $[HCO_3^-]$ by definition (see (8.2.5), whereas for $pK_1 < pH < pK_2 = -\log K_2$, HCO_3^- is the species dominating *DIC*. At $pH = pK_2$, $[HCO_3^-] = [CO_3^{2-}]$, and at $pH > pK_2$, $[CO_3^{2-}]$ dominates. Since the ocean has a mean surface pH of slightly above 8, in

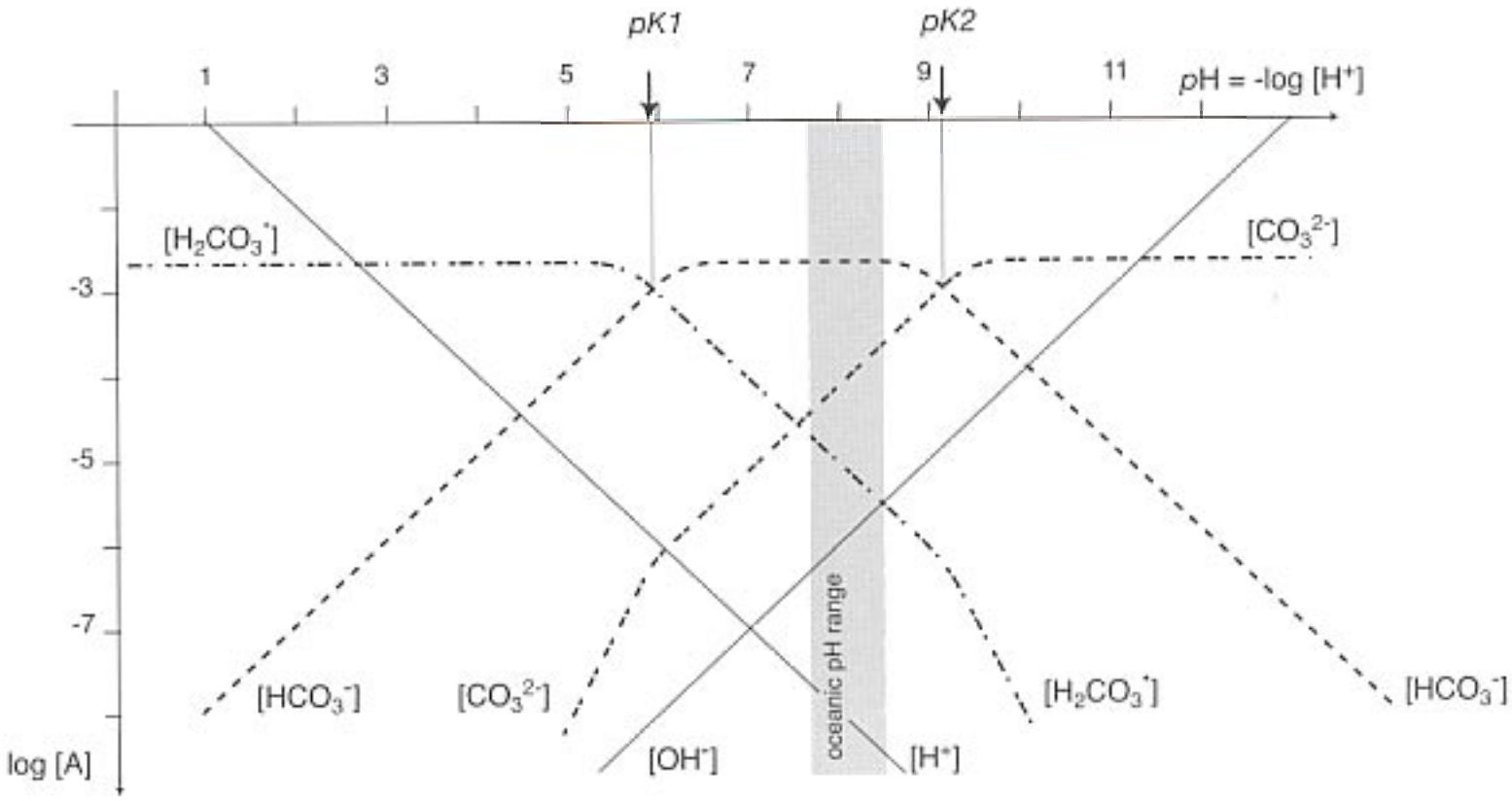

FIGURE 8.2.1: Plot of the concentrations of $H_2CO_3^*$, HCO_3^-, and CO_3^{2-} as functions of $pH = -\log_{10}[H^+]$. Note that the vertical axis is logarithmic to the base 10 as well. The concentrations are plotted for a *DIC* concentration of 2000 μmol kg^{-1}. By definition, the crossing point of an acid/base pair is equal to the pK of the corresponding dissociation constant.

between pK_1 and pK_2, we see immediately why HCO_3^- is the most important species present in seawater. Oceanic pH is also closer to pK_2 than to pK_1, so that it also becomes evident why CO_3^{2-} is the second most dominant inorganic carbon species, and why the concentration of $H_2CO_3^*$ is so small.

A note at the end: We usually normalize *DIC* and *Alk* to a constant salinity in order to remove the effect of freshwater fluxes. As described above, these normalized concentrations are denoted by the symbols *sDIC* and *sAlk*. The motivation of this normalization is that freshwater contains very little *DIC* and *Alk*, so that the addition of freshwater, for example, leads to a decrease of the *DIC* and *Alk* concentration, i.e., it dilutes the concentration of all chemical species present in seawater in direct proportion of the dilution of salinity. The opposite effect occurs if an excess of evaporation over precipitation leads to a net removal of freshwater from the surface ocean. Thus, net freshwater exchange at the surface leads to variations in *DIC* and *Alk* that can mask the "chemical" changes that we are mostly interested in, i.e., those changes driven by ocean biology, chemistry, and mixing/transport. For consistency, salinity normalization should be done for all other chemical properties that we investigate. However, since the concentration variations of most chemical properties of interest are large relative to their mean concentration, salinity normalization has little influence on these properties, and is therefore often neglected. By contrast, typical chemically or biologically induced variations in *DIC* and *Alk* are much smaller than their mean concentrations, so that freshwater flux variations have a much larger impact on these two properties. We therefore generally apply the salinity normalization to *DIC* and *Alk* observations.

8.3 The Surface Ocean

Having reviewed the most important aspects of marine carbon chemistry, we are now ready to tackle the problems we outlined at the beginning of this chapter. We start with the problem of what controls the annual mean spatial distribution of the surface pCO_2 and then proceed to a discussion of its seasonal variability.

Annual Mean Distribution

The simplest answer to what controls surface pCO_2 is that it is determined by the concentration of $H_2CO_3^*$ in the water and the CO_2 solubility, K_0, i.e.,

$$pCO_2 = \frac{[H_2CO_3^*]}{K_0}. \tag{8.3.1}$$

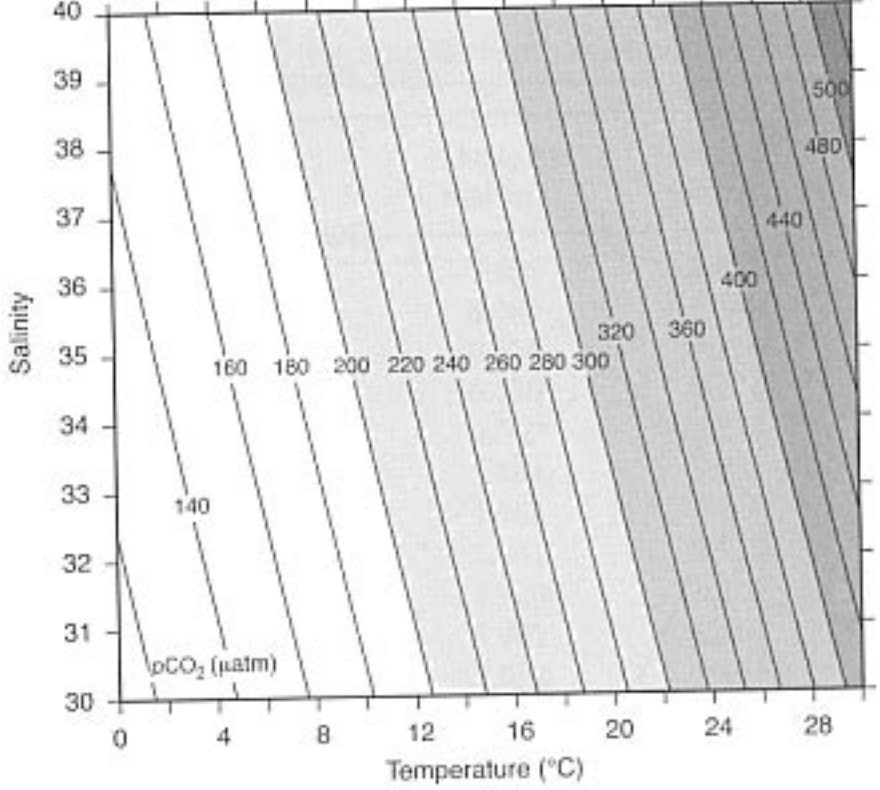

FIGURE 8.3.1: Plot of the partial pressure of CO_2 (pCO_2) as a function of temperature and salinity for constant *DIC* and *Alk*. Shown are the results for a typical surface water sample with an alkalinity of 2322 μmol kg^{-1} and a *DIC* content of 2012 μmol kg^{-1}.

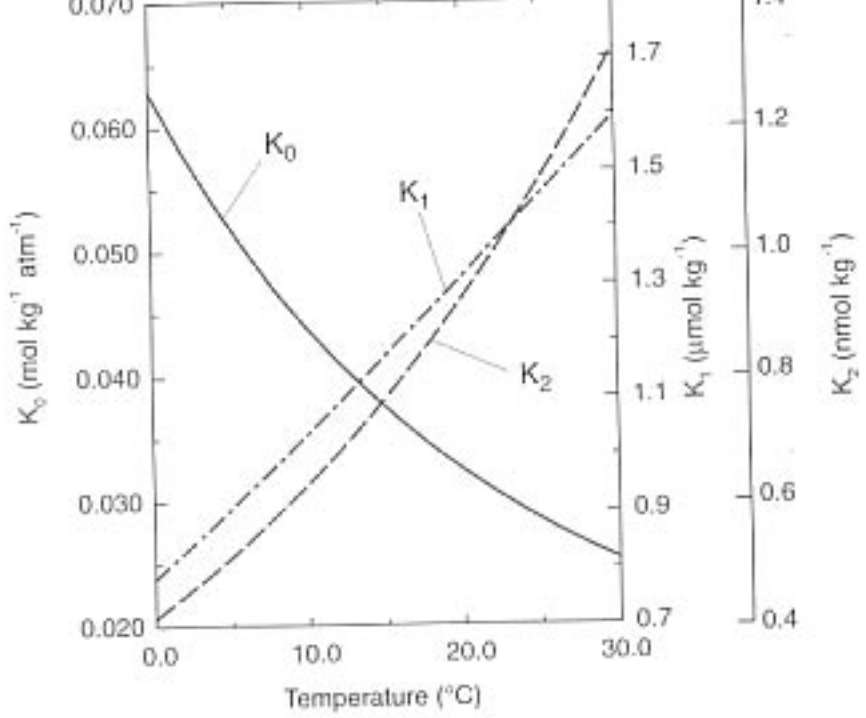

FIGURE 8.3.2: Plot of the CO_2 solubility (K_0), and of the first and second dissociation constants of carbonic acid (K_1 and K_2) as a function of temperature.

However, since $H_2CO_3^*$ constitutes only a very small fraction of the *DIC* pool, the bicarbonate and carbonate ions, rather than $H_2CO_3^*$, are ultimately controlling the pCO_2. To demonstrate this, we recast equations (8.2.4), (8.2.5), and (8.2.6) to relate the partial pressure of CO_2 in seawater to variations in carbonate and bicarbonate ions, and the three equilibrium constants K_0, K_1, and K_2,

$$pCO_2 = \frac{K_2}{K_0 \cdot K_1} \frac{[HCO_3^-]^2}{[CO_3^{2-}]} \tag{8.3.2}$$

In order to facilitate our discussion, we use approximations (8.2.17) and (8.2.18) to replace the bicarbonate and carbonate ion concentrations with *DIC* and *Alk*:

$$pCO_2 \approx \frac{K_2}{K_0 \cdot K_1} \frac{(2 \cdot DIC - Alk)^2}{Alk - DIC} \tag{8.3.3}$$

From consideration of (8.3.3), we see that the question of what controls the surface pCO_2 distribution is more complex than first suggested by (8.3.1). The best way to answer the question is to break it into three parts: (i) what controls the ratio of the equilibrium constants, $K_2/(K_0 \cdot K_1)$, (ii) what controls the *DIC* concentration, and (iii) what controls the *Alk* concentration.

We know from table 8.2.2 that the three equilibrium constants K_0, K_1, and K_2 are a function of temperature and salinity. The first of these questions can thus be readily answered by considering how the pCO_2 of a water parcel changes with temperature and salinity while keeping *DIC* and *Alk* constant. It turns out that the answer for the other two questions cannot be given independently of each other. The concentration of *DIC* is affected by air-sea gas exchange and by biological processes, whereas *Alk* is only affected by ocean biology. It it thus more convenient to separate the controls on surface ocean pCO_2 into physical processes and biological processes.

PHYSICAL PROCESSES

We start our discussion by considering how the pCO_2 varies with temperature and salinity while keeping *DIC* and *Alk* constant. As shown in figure 8.3.1, the isolines of pCO_2 are almost vertical over the oceanic range of temperature and salinity, indicating a much greater sensitivity to temperature than to salinity variations. It turns out that about two-thirds of the temperature sensitivity of pCO_2 is a result of the strong temperature dependence of the solubility K_0 (figure 8.3.2), while the contribution of the ratio of the dissociation constants K_2/K_1 explains the remaining third. Since K_0 is relatively insensitive to salinity, about 70% of the salinity dependence of pCO_2 is governed by the ratio K_2/K_1.

Takahashi et al. [1993] provide a useful relationship that summarizes the temperature sensitivity of pCO_2 in a closed system, i.e., one where the concentration of *DIC* and *Alk* remain constant. They determined this sensitivity experimentally and found that a logarithmic dependence gave accurate results, thus

$$\frac{1}{pCO_2} \frac{\partial pCO_2}{\partial T} = \frac{\partial \ln pCO_2}{\partial T} \approx 0.0423^\circ C^{-1} \tag{8.3.4}$$

TABLE 8.3.1
Summary of the most important pCO_2 sensitivities in seawater

Parameter	*Definition*	*Mean Global*	*Mean High Latitudes*	*Mean Low Latitudes*
Temperature	$\frac{1}{pCO_2}\frac{\partial pCO_2}{\partial T}$	$0.0423°C^{-1}$	$0.0423°C^{-1}$	$0.0423°C^{-1}$
Salinity	$\gamma_S = \frac{S}{pCO_2}\frac{\partial pCO_2}{\partial S}$	1	1	1
DIC	$\gamma_{DIC} = \frac{DIC}{pCO_2}\frac{\partial pCO_2}{\partial DIC}$	10	13.3	9.5
Alk	$\gamma_{Alk} = \frac{Alk}{pCO_2}\frac{\partial pCO_2}{\partial Alk}$	−9.4	−12.6	−8.9
Freshwater†	$\gamma_{freshwater} = \frac{S}{pCO_2}\frac{\partial pCO_2}{\partial S}\Big\|_{freshwater} = \gamma_S + \gamma_{DIC} + \gamma_{Alk}$	1.6	1.7	1.6

† See chapter 10 for derivation.

Similarly, one finds for the salinity dependence of pCO_2,

$$\gamma_S = \frac{S}{pCO_2}\frac{\partial pCO_2}{\partial S} = \frac{\partial \ln pCO_2}{\partial \ln S} \approx 1 \qquad (8.3.5)$$

For example, if we take a water parcel with an initial pCO_2 of 300 μatm at 20°C and with a salinity of 35, a one-degree warming increases pCO_2 by approximately 13 μatm, whereas a salinity increase of 1 results in a pCO_2 increase of 9 μatm. Since temperature varies in the oceans by about 30°C, whereas salinity varies only by about 7, temperature rather than salinity has to be regarded as the dominant physical factor controlling pCO_2. A note of caution, however. The above salinity dependence is for constant *DIC* and *Alk*. Therefore, the CO_2 change given by (8.3.5) includes only the influence of salinity on the dissociation constants. Variations in salinity in the surface ocean, however, are mostly driven by changes in the balance between evaporation and precipitation. Therefore, if one is interested in using salinity as a tracer of the impact of the freshwater balance on pCO_2, one needs to take into account freshwater-induced *DIC* and *Alk* changes in addition to the direct salinity effect. We will show in chapter 10 how one can calculate this freshwater balance effect on pCO_2. We demonstrate there that the net effect of freshwater changes on the pCO_2 sensitivity is to increase the pure salinity-driven pCO_2 changes by about 60% (see table 8.3.1).

The next issue we consider is what happens to the carbon system if we permit gas exchange of CO_2 to occur while keeping *Alk* constant. Gas exchange will change the *DIC* concentration, but not *Alk*. The influence of air-sea gas exchange can be assessed with the following thought experiment taken from *Broecker and Peng* [1982] (see figure 8.3.3). We consider two extreme scenarios. In the first case, air-sea exchange is assumed to be sluggish compared to the residence time of water at the sea surface (figure 8.3.3a). Such a scenario is equivalent to the closed system that was discussed in the previous paragraph. Since air-sea exchange is severely restricted, *DIC* is nearly constant throughout the ocean and pCO_2 changes according to its temperature sensitivity of about 4% per degree centigrade. This results in the low latitudes having an oceanic pCO_2 twice as large as the high latitudes.

In the second scenario, air-sea gas exchange is assumed to be very rapid, so that oceanic pCO_2 comes close to equilibrium with atmospheric CO_2 everywhere (figure 8.3.3b). Since oceanic pCO_2 is now almost constant everywhere, oceanic *DIC* has to change in order maintain chemical equilibrium. What is the magnitude and direction of this change? We have learned that the factor $K_2/(K_0 \cdot K_1)$ increases with increasing temperatures. Therefore, in order to maintain the same oceanic pCO_2, we infer from (8.3.3) that *DIC* has to decrease with increasing temperature. Therefore, we find higher *DIC* values in the high-latitude ocean and lower *DIC* in the low latitudes.

Where in the range between these two extremes would we expect an ocean with realistic gas exchange to lie? This depends essentially on the timescale of air-sea gas exchange relative to the timescale of processes perturbing the local equilibrium. We have seen in chapter 3 that the air-sea gas exchange timescale for many gases is of the order of days to a few weeks. This is short relative to most perturbations, so that the oceanic partial pressure of these gases is usually very close to equilibrium with the atmosphere, as observed, for example, for oxygen (see figure 3.1.2). However, as we also saw in chapter 3, the gas exchange timescale of CO_2 is of the order of 6 months. Why is this the case? We were previously able to give only a partial explanation, but now we know enough about CO_2 chemistry to fill in this gap.

The time rate of change of any gas, A, in a surface mixed layer box that exchanges only with the atmosphere is given by

$$\frac{\partial [A]_w}{\partial t} = -\frac{\partial \Phi}{\partial z} = \frac{k_w}{z_{ml}}([A]_a - [A]_w) \qquad (8.3.6)$$

where k_w is the gas exchange coefficient (for CO_2 typically 20 cm hr^{-1}) and z_{ml} is the thickness of the mixed layer box (see also chapter 3). If we assume for the moment that the atmospheric concentration is fixed, (8.3.6) is a first-order differential equation in $[A]_w$. Its time-dependent solution is therefore an exponential with a timescale given by $(k_w/z_{ml})^{-1}$:

$$\tau = \frac{z_{ml}}{k_w} = \frac{z_{ml}}{20\,\text{cm hr}^{-1}} = 5\,\text{hr m}^{-1}\, z_{ml} \qquad (8.3.7)$$

For a 40 m-deep surface mixed layer, the timescale amounts to about 8 days.

Because CO_2 needs to equilibrate with the entire *DIC* pool in the surface ocean and not just with the $H_2CO_3^*$ pool, the timescale for CO_2 is much longer. When CO_2 enters the ocean from the atmosphere, approximately 19 out of 20 molecules react with carbonate (the strongest base of the CO_2 system) to form two bicarbonate ions, i.e.,

$$H_2CO_3^* + CO_3^{2-} \rightleftharpoons 2HCO_3^- \qquad (8.3.8)$$

leaving behind only one molecule as $H_2CO_3^*$.

For CO_2, we therefore have to consider the time rate of change of all inorganic carbon species, i.e.,

$$\frac{\partial DIC}{\partial t} = \frac{\partial DIC}{\partial [H_2CO_3^*]} \frac{\partial [H_2CO_3^*]}{\partial t} = \frac{k_w}{z_{ml}}([H_2CO_3^*]_a - [H_2CO_3^*]) \qquad (8.3.9)$$

Solving for the time rate of change of $[H_2CO_3^*]$ results in

$$\frac{\partial [H_2CO_3^*]}{\partial t} = \left(\frac{\partial DIC}{\partial [H_2CO_3^*]}\right)^{-1} \frac{k_w}{z_{ml}}([H_2CO_3^*]_a - [H_2CO_3^*]) \qquad (8.3.10)$$

This equation is analogous to (8.3.6), except that the e-folding timescale for equilibration of a perturbation in the CO_2 system is given by

$$\tau = \frac{\partial DIC}{\partial [H_2CO_3^*]}\left(\frac{z_{ml}}{k_w}\right) \approx 20\frac{z_{ml}}{k_w} \qquad (8.3.11)$$

Here, we have used a partial derivative $\partial DIC/\partial[H_2CO_3^*]$ of 20 based on solving the carbon chemistry equations. This derivative indicates that only about 1 molecule of CO_2 in 20 molecules entering or leaving the ocean stays as $H_2CO_3^*$. Why is this the case? One might be tempted to argue that this partial derivative should be about equal to the concentration ratio of $DIC/[H_2CO_3^*] \approx 200$. However, as it turns out, variations in the concentration of the carbonate ion are the primary determinant of this partial derivative (see figure 8.3.4).

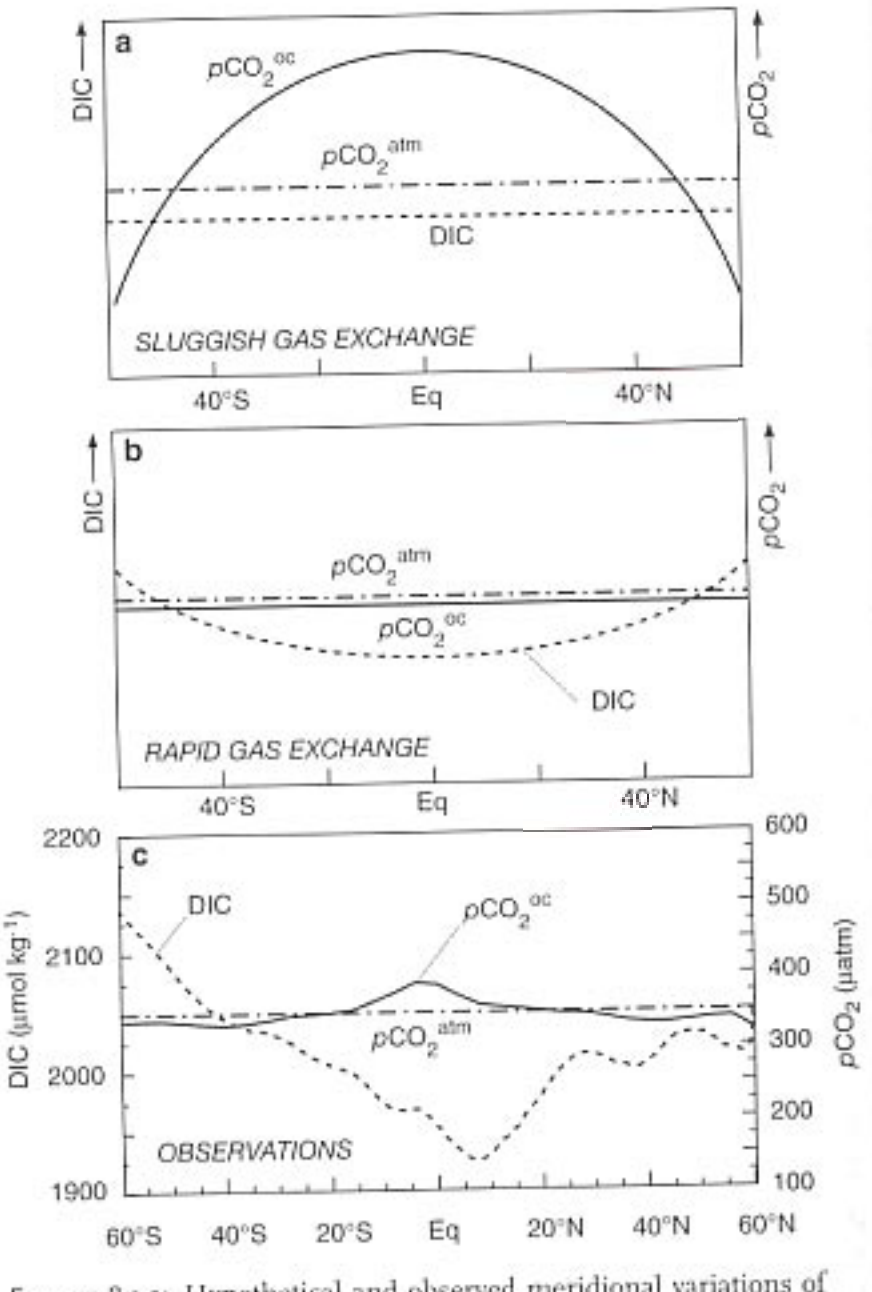

FIGURE 8.3.3: Hypothetical and observed meridional variations of pCO_2 and *DIC* in the surface ocean. (a) Hypothetical distribution in a case where gas exchange is very slow. It is assumed that no biological processes take place and that therefore *Alk* remains constant [*Broecker and Peng*, 1982]. (b) As in (a), but for a case with very rapid gas exchange. (c) Observed zonal mean variations of pCO_2 and *DIC*. Based on the pCO_2 climatology of *Takahashi et al.* [2003] and the GLODAP climatology of *Key et al.* [2004].

This can best be understood by reaction (8.3.8). The fraction of the total number of CO_2 molecules added to the ocean that are converted to HCO_3^- and consequently do not increase the $H_2CO_3^*$ pool depends on the availability of CO_3^{2-}. As the concentration of carbonate is about 15 to 20 times higher than that of $H_2CO_3^*$, the partial derivative is of the order of 20 rather than 200. A more rigorous derivation is given in panel 8.3.1.

We now have established that the characteristic timescale for air-sea exchange of CO_2 is of the order of 6 months, but still have not answered the question of where between the two extreme scenarios discussed above the real ocean lies. Are 6 months long or short compared to the average residence time of waters near the surface and the timescale of perturbations? The ΔpCO_2 observations in figure 8.1.1 suggest that the real ocean lies between the two scenarios: the pCO_2 is clearly out of equilibrium with the atmosphere, but

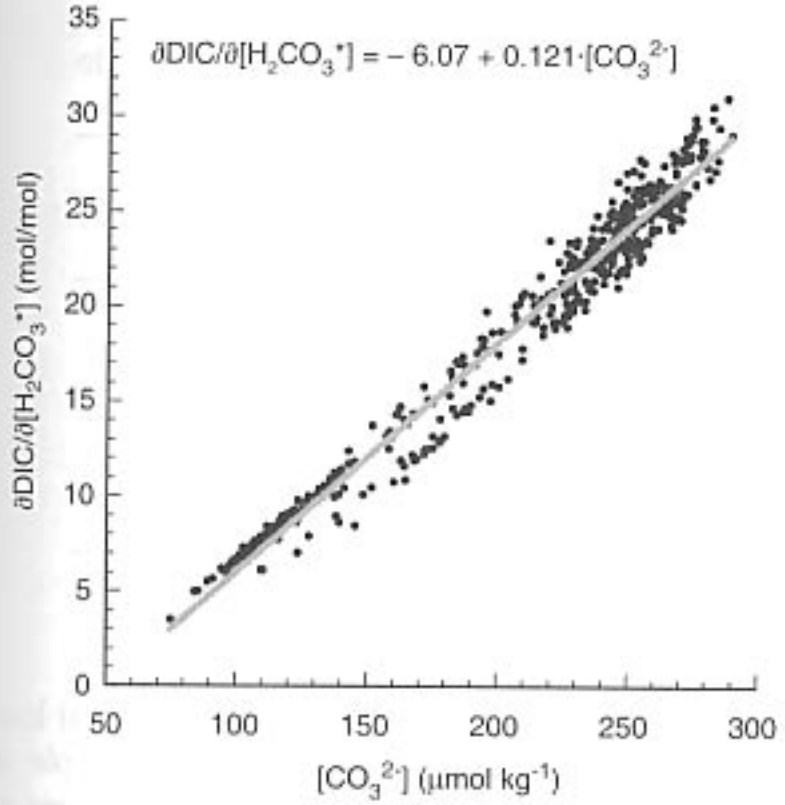

FIGURE 8.3.4: Plot of the partial derivative of *DIC* with respect to $[H_2CO_3^*]$. ($\partial DIC/\partial[H_2CO_3^*]$) versus the concentration of the carbonate ion $[CO_3^{2-}]$. Plotted are the surface ocean (< 50 m) data as obtained during the GEOSECS program.

nowhere near the factor of two between the coldest and warmest waters that would be expected from (8.3.4). In fact, observations of *DIC* suggest that the real ocean is closer to the rapid gas exchange case than it is to the sluggish one (figure 8.3.3c).

BIOLOGICAL PROCESSES

We now turn to a consideration of the influence of biology, which changes both the *DIC* and *Alk* distributions. The most important biological processes altering the concentration of *DIC* in the ocean are the photosynthetic uptake of CO_2 to form organic matter, and the reverse processes of respiration and remineralization (see reaction (4.2.4)):

$$106CO_2 + 16NO_3^- + HPO_4^{2-} + 78H_2O + 18H^+ \rightleftharpoons C_{106}H_{175}O_{42}N_{16}P + 150O_2 \qquad (8.3.12)$$

We have recast the original reaction (4.2.4) to emphasize that NO_3^- and HPO_4^{2-} rather than HNO_3 and H_3PO_4, respectively, are the dominant chemical species present in seawater. Thus, in addition to decreasing the concentration of *DIC*, the formation of organic matter also decreases the concentration of the free protons, $[H^+]$, and therefore increases alkalinity (see definition (8.2.8)) [*Brewer et al.*, 1975]. Most of these protons are consumed by the assimilatory reduction of nitrate to organic nitrogen (see figure 5.1.5). The influence of the nitrate uptake on *Alk* can also be understood by considering the alternative definition of *Alk* (8.2.9), which shows that a decrease in the nitrate concentration increases *Alk*. While the dominant species at the pH of seawater is indeed HPO_4^{2-}, it is not well established whether this is actually the species taken up by phytoplankton or rather the uncharged H_3PO_4.

Panel 8.3.1: Derivation of the partial derivative $\partial DIC/\partial[H_2CO_3^*]$

We want to demonstrate the fact that the partial derivative $\partial DIC/\partial[H_2CO_3^*]$ is controlled by the CO_3^{2-} ion concentration and is about 20. We start by inserting the two approximations for HCO_3^- and CO_3^{2-} into (8.3.2) and by replacing $K_0 \cdot pCO_2$ with $[H_2CO_3^*]$. This gives

$$[H_2CO_3^*] \approx \frac{K_2}{K_1}\frac{(2 \cdot DIC - Alk)^2}{Alk - DIC} \qquad (1)$$

The partial derivative of *DIC* with respect to $[H_2CO_3^*]$ is equal to the inverse of the partial derivative of $[H_2CO_3^*]$ with respect to *DIC*. This gives

$$\frac{\partial DIC}{\partial[H_2CO_3^*]} = \left(\frac{\partial[H_2CO_3^*]}{\partial DIC}\right)^{-1} \approx \left(\frac{K_2}{K_1}\frac{\partial}{\partial DIC}\left(\frac{(2 \cdot DIC - Alk)^2}{Alk - DIC}\right)\right)^{-1} \qquad (2)$$

Computing the derivative and substituting the *DIC* and *Alk* approximations back into the resulting equation gives

$$\frac{\partial DIC}{\partial[H_2CO_3^*]} \approx \frac{K_1}{K_2}\frac{[CO_3^{2-}]^2}{4[HCO_3^-][CO_3^{2-}] + [HCO_3^-]^2} \qquad (3)$$

Inserting typical surface ocean concentrations for bicarbonate and carbonate gives a partial derivative of 20.

It is, however, not yet evident why the carbonate ion content is the main controlling factor. In order to demonstrate this, we are going to simplify the equation even further. As the concentration of CO_3^{2-} is much smaller than the concentration of HCO_3^- (see table 8.2.4), the first part of the denominator is much smaller than the second, i.e., $4[HCO_3^-][CO_3^{2-}] \ll [HCO_3^-]^2$ and can thus be neglected. This results in:

$$\frac{\partial DIC}{\partial[H_2CO_3^*]} \approx \frac{K_1}{K_2}\frac{[CO_3^{2-}]^2}{[HCO_3^-]^2} \approx \frac{[CO_3^{2-}]}{[H_2CO_3^*]} \approx 20 \qquad (4)$$

where we have made use of (8.3.2) to replace $(K_2/K_1) \cdot ([HCO_3^-]^2/[CO_3^{2-}])$ with $[H_2CO_3^*]$. Note from equation (2) in this panel that this partial derivative is largely independent of temperature, but is largely controlled by variations in the *Alk*-to-*DIC* ratio.

TABLE 8.3.2
Changes in pCO_2 as a typical water parcel from the deep sea is moved to the surface and adjusted to typical low-latitude surface values (see table 8.2.4 for values)

	(1) *Deep Water*	(2) *Move to Surface*	(3) *Warm Up*	(4) *Formation of Organic Matter*	(5) *Formation of $CaCO_3$*
Pressure (atm)	400	1	1	1	1
Temp (°C)	1.8	1.8	23	23	23
PO_4 (μmol kg^{-1})	2.1	2.1	2.1	0	0
DIC (μmol kg^{-1})	2298	2298	2298	2058	1994
Alk (μmol kg^{-1})	2400	2400	2400	2433	2305
pCO_2 (μatm)		510	1220	293	348

The changes in *DIC* and *Alk* due to the removal of organic matter and the loss of $CaCO_3$ were calculated using the stoichiometry of Anderson *and* Sarmiento [1994].

As we have discussed in detail in chapter 4, organic matter is produced in the uppermost sunlit layers of the ocean. A fraction of the organic matter is exported to the deeper layers through settling particles or advection of dissolved organic carbon. This leads to a net consumption of CO_2 in these upper layers. Upon remineralization of this organic matter in the deeper layers, this CO_2 is returned to the seawater. Thus these biological processes lead to a net transfer of inorganic carbon from the surface into the abyss. This process is often termed the "soft-tissue" pump [*Volk and Hoffert*, 1985]. In a steady state, this net downward flux has to be compensated by a net upward flux of inorganic carbon by transport processes.

The second biological reaction of great importance for carbon cycling is the biogenic formation and dissolution of calcite or aragonite:

$$Ca^{2+} + CO_3^{2-} \rightleftharpoons CaCO_3 \tag{8.3.13}$$

The formation and dissolution of mineral calcium carbonates changes *Alk* twice as much as it changes *DIC*. This is best understood by considering the charge balance definition of *Alk* (equation (8.2.9)), which shows that a 1 mol reduction in the concentration of Ca^{2+} results in a 2 mol change in *Alk*. Mineral calcium carbonate shells are formed in the upper layers of the ocean mainly by three groups of organisms: coccolithophorids, foraminifera, and pteropods. The first group are phytoplankton, whereas the second and third groups are zooplankton (see panels 4.2.2 and 4.2.3, respectively). Upon the death of these organisms, their shells sink and eventually dissolve, either in the water column or in the sediments, except for a small fraction that is buried permanently. The net effect of this process is a downward transport of *DIC* and *Alk* from the surface ocean into the abyss. This process is often dubbed the "carbonate pump."

The large influence of the biological pumps on pCO_2 can be dramatically demonstrated by the following thought experiment after *Broecker and Peng* [1982] (see table 8.3.2). We take a typical deep water parcel and bring it to the surface, adjusting its properties to typical low-latitude values (see table 8.2.4). After the sample is warmed from 1.8°C to 23°C, it has a pCO_2 in excess of 1200 μatm. Next, we remove all phosphate present and form organic matter, thus removing *DIC* from the water and adding *Alk* in proportion to the change in nitrate, assuming a constant nitrate to phosphate ratio of 16:1. What pCO_2 does this water parcel have after these changes? In order to compute the answer, we have to know the sensitivity of pCO_2 to changes in *DIC* and *Alk*.

We estimate the sensitivity of pCO_2 to changes in the *DIC* and *Alk* content of seawater by considering (8.3.3). This equation tells us that pCO_2 decreases when *DIC* decreases, but that pCO_2 increases for a decrease in *Alk*. The magnitude of these changes in pCO_2 depends strongly on the relative proportions of the *DIC* and *Alk* concentrations (see figure 8.3.5). To evaluate this more quantitatively, we investigate the following two dimensionless sensitivities:

$$\gamma_{DIC} = \frac{DIC}{pCO_2}\frac{\partial pCO_2}{\partial DIC} = \frac{\partial \ln pCO_2}{\partial \ln DIC} \tag{8.3.14}$$

$$\gamma_{Alk} = \frac{Alk}{pCO_2}\frac{\partial pCO_2}{\partial Alk} = \frac{\partial \ln pCO_2}{\partial \ln Alk} \tag{8.3.15}$$

We will refer to the sensitivity of pCO_2 to changes in *DIC* as the "buffer factor" or "Revelle factor" [*Takahashi et al.*, 1980] after Roger Revelle, who was among the first to point out the importance of this sensitivity for the oceanic uptake of anthropogenic CO_2. By analogy, we will refer to the alkalinity sensitivity, γ_{Alk}, as the alkalinity factor. We can estimate these factors by calculating the partial derivatives using the approximation (8.3.3). With some modifications we arrive at:

$$\gamma_{DIC} \approx \frac{3 \cdot Alk \cdot DIC - 2 \cdot DIC^2}{(2 \cdot DIC - Alk)(Alk - DIC)} \tag{8.3.16}$$

$$\gamma_{Alk} \approx -\frac{Alk^2}{(2 \cdot DIC - Alk)(Alk - DIC)} \tag{8.3.17}$$

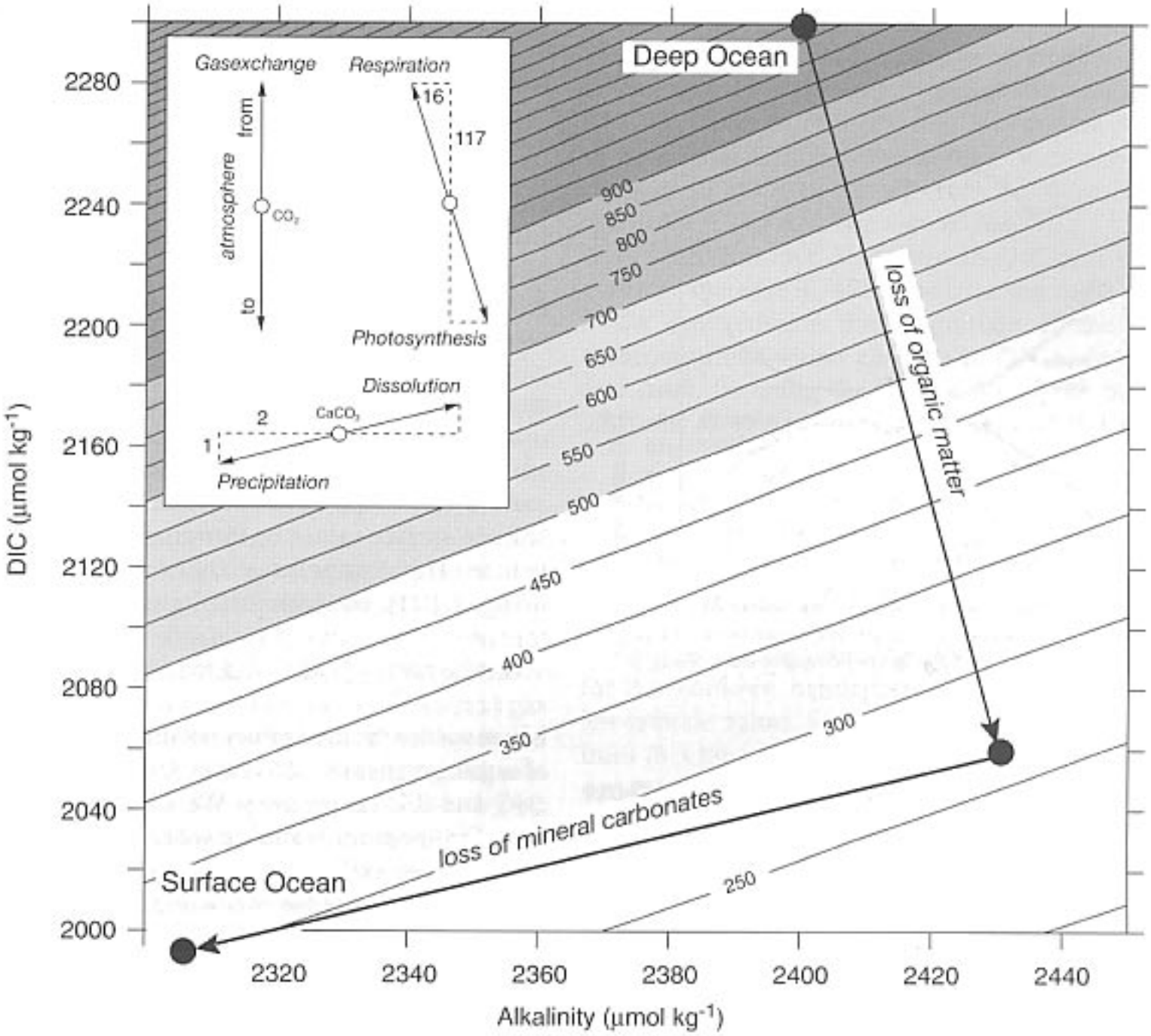

FIGURE 8.3.5: Plot of the CO_2 partial pressure as a function of *Alk* and *DIC* for a typical surface temperature (20°C) and salinity (35), computed from the equations given in table 8.2.1. Also shown is a simplified representation of the composition changes caused by biological processes. Water of average deep water composition is brought to the surface, and is warmed up to 20°C (point 1). It undergoes photosynthesis (point 1 to 2) and calcium carbonate precipitation (point 2 to 3). The inset shows the vectors of the different processes affecting *DIC* and *Alk*, and hence also pCO_2.

Inserting typical values for the surface ocean yields a buffer factor (γ_{DIC}) of about 12 and an alkalinity factor (γ_{Alk}) of about −10. These factors, computed with the full chemistry including borate, are about 10 and −9.4, respectively, meaning that pCO_2 increases by about 10% when *DIC* is increased by 1%, whereas pCO_2 decreases by about 9.4% when *Alk* is increased by 1%.

It is important to recognize that the magnitudes of these two factors are not a direct function of temperature. Instead, these factors are mainly determined by the relative concentrations of *DIC* and *Alk* as evident from (8.3.16) and (8.3.17) [*Takahashi et al.*, 1980]. Because *DIC* concentrations tend to correlate with temperature (see figure 8.1.4b), while surface *Alk* is spatially more homogeneous, the resulting correlation of the *DIC*-to-*Alk* ratio with temperature leads to a correlation of the buffer factor with temperature as well. This correlation between the buffer factor and temperature is a result of temperature causing some of the variations in *DIC* and not because of temperature directly driving variations in the buffer factor.

The gas exchange thought experiment that we used above (figure 8.3.3) provides a framework to illustrate this. We assume in both the rapid and sluggish gas exchange cases a spatially uniform alkalinity. In the sluggish gas exchange case, *DIC* would be spatially uniform as well, making the buffer factor essentially constant. In the rapid gas exchange case, the temperature variations are fully expressed in the surface concentration of *DIC*, leading to strong meridional variations in the *DIC*-to-*Alk* ratio. This also causes strong meridional variations in the buffer factor. The real ocean is somewhat closer to the fast gas exchange case, explaining the observed meridional variations in the buffer factor. As we will see

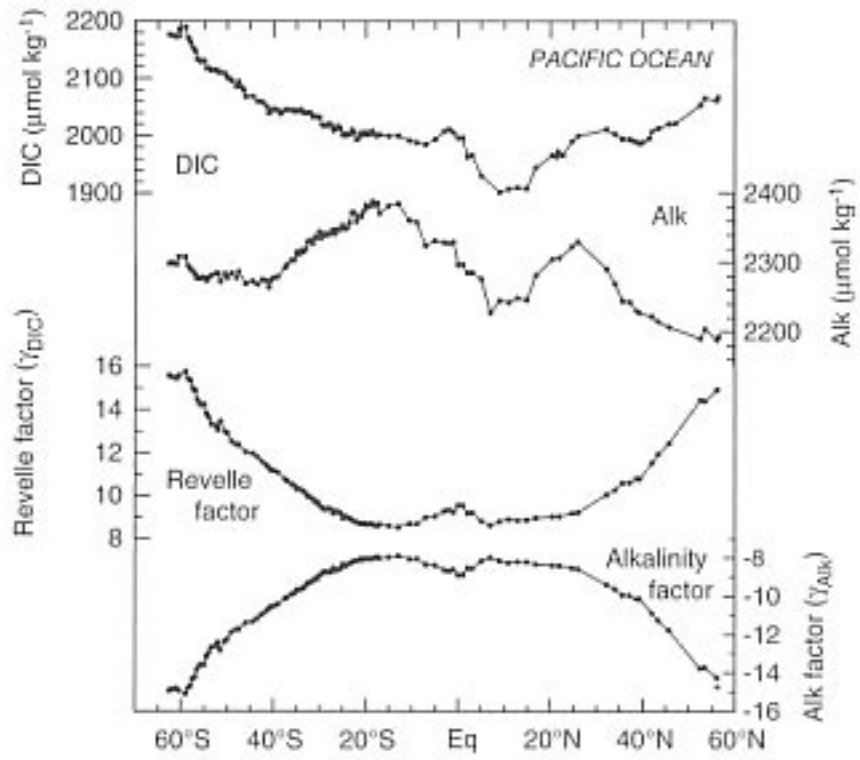

FIGURE 8.3.6: Meridional profiles of *DIC*, *Alk*, buffer factor (γ_{DIC}), and the alkalinity factor (γ_{Alk}) in the surface ocean of the Pacific. Based on data from the WOCE P16 meridional section along approximately 160°W.

in chapter 10, these spatial variations in the buffer factor have important implications for the uptake and storage of anthropogenic CO_2.

In summary, typical values for γ_{DIC} and γ_{Alk} in the surface oceans are

$$\gamma_{DIC} \approx 10 \begin{cases} 9.5 \text{ low latitudes} \\ 13.3 \text{ high latitudes} \end{cases} \tag{8.3.18}$$

$$\gamma_{Alk} \approx -9.4 \begin{cases} -8.9 \text{ low latitudes} \\ -12.6 \text{ high latitudes} \end{cases} \tag{8.3.19}$$

(see also table 8.3.1 and figure 8.3.6).

Having established the sensitivity of pCO_2 to *DIC* and *Alk*, we can now return to our thought experiment shown in table 8.3.2. In this experiment, we wanted to know how the biologically induced changes in *DIC* and *Alk* affect pCO_2. We estimate the change in pCO_2 by assuming that the effects of changes in *DIC* and *Alk* are independent of each other, and therefore additive. Solving both (8.3.14) and (8.3.15) for $d\ln pCO_2$ and then integrating the left and the right sides of the resulting equations gives:

$$\int d \ln pCO_2 = \gamma_{DIC} \int d \ln DIC + \gamma_{Alk} \int d \ln Alk \tag{8.3.20}$$

Integrating (8.3.20) from an initial state (i) to a final state (f) and inserting mean ocean values for γ_{DIC} and γ_{Alk} yields:

$$\ln pCO_2^f \approx \ln pCO_2^i + 10\,(\ln DIC^f - \ln DIC^i) - 9.4\,(\ln Alk^f - \ln Alk^i) \tag{8.3.21}$$

We estimate the final state f of *DIC* and *Alk* as a result of the formation of organic matter from the change in phosphate, $\Delta PO_4^{3-} = [PO_4^{3-}]^f - [PO_4^{3-}]^i$:

$$DIC^f = DIC^i + r_{C:P}\Delta PO_4^{3-} \tag{8.3.22}$$

$$Alk^f = Alk^i - r_{N:P}\Delta PO_4^{3-} \tag{8.3.23}$$

where $r_{C:P} = 117$ and $r_{N:P} = 16$ are the stoichiometric ratios of reaction (8.3.12). On the basis of approximation (8.3.21), we calculate that the removal of all phosphate present in this deep ocean water parcel, i.e., $\Delta PO_4^{3-} = -[PO_4^{3-}]^i$, lowers the pCO_2 by more than 900 μatm. Our approximate calculation is remarkably close to an estimate on the basis of a full carbon chemistry model, which predicts a decrease of 927 μatm (table 8.3.2).

As a last step, we adjust alkalinity to typical low-latitude surface values by forming mineral calcium carbonate. The change in pCO_2 can again be estimated using (8.3.21), but with DIC^f given by

$$DIC^f = DIC^i + \frac{1}{2}(Alk^f - Alk^i) \tag{8.3.24}$$

where we use the final values obtained after the formation of organic matter (8.3.22) and (8.3.23) as our initial values, DIC^i and Alk^i, respectively. We set Alk^f to the observed value for low-latitude surface waters (see table 8.2.4). The formation of carbonates increases pCO_2 slightly, such that a final pCO_2 value of about 350 μatm is computed, close to the atmospheric pCO_2 at the time when these *DIC* and *Alk* measurements were obtained (1988–1996).

VECTOR DIAGRAMS

Another way to depict the various processes that affect pCO_2 in the surface ocean is as vectors in a plot of *DIC* versus *Alk* (see inset in figure 8.3.5) [*Baes*, 1982]. The three major processes discussed form the following vectors:

1. *Gas exchange:* When CO_2 is transferred across the air-sea interface, the oceanic *DIC* changes proportionally, whereas *Alk* remains unaffected. Hence the vector is a vertical line with a length that is directly proportional to the number of molecules transferred.

2. *Soft-tissue pump:* The formation of organic matter reduces *DIC* and increases *Alk* proportional to the ratio of carbon to nitrogen, or about −117:16. Thus on a *DIC* versus *Alk* diagram, the vector forms a line with a slope of about −7.3.

3. *Carbonate pump:* When calcium carbonate is precipitated or dissolved, the water composition is changed along a line of slope ½ on the diagram. As we have seen above, this is because the carbonate ion contributes two moles to *Alk* for each mole of *DIC*.

A good example of the power of these vector diagrams is the depiction of our thought experiment of a deep water sample that was brought to the surface and adjusted to typical low-latitude values. Figure 8.3.5

shows a summary of the changes in pCO_2 that occur as *DIC* and *Alk* are changed.

Seasonal Variability

Summer-winter differences of surface ocean pCO_2 amount in many extratropical regions to more than 40 μatm (figure 8.3.7a) and are therefore comparable to the spatial variability of annual mean pCO_2 (figure 8.1.1). Figure 8.3.7a also reveals a distinct difference between the regions poleward of 40°, which generally show a decrease in surface ocean pCO_2 from winter to summer, and the subtropical latitudes, which experience an increase in surface ocean pCO_2 over the same period (cf. *Takahashi et al.* [2002]). What are the causes of these seasonal variations?

We learned from our discussion of (8.3.3) above that the processes that control surface ocean pCO_2 are temperature and salinity, which act through their influence on the equilibrium constants, $K_2/(K_0 \cdot K_1)$; and processes that affect the concentrations of *DIC* and *Alk*, such as gas exchange, biology, and lateral and vertical transport and mixing. We start our discussion by considering the seasonal variations in sea surface temperature. We neglect seasonal variations in salinity, as they are negligible.

We have seen that oceanic pCO_2 changes by about 13 μatm for each degree of warming or cooling. This permits us to estimate the effect of seasonal changes in SST on pCO_2 simply by multiplying the observed seasonal SST changes, ΔSST, by this factor, i.e.,

$$\Delta pCO_2\big|_{thermal} \approx pCO_2 \cdot 0.0423(^\circ C)^{-1} \cdot \Delta SST \qquad (8.3.25)$$

The "thermally" forced pCO_2 amplitude, $\Delta pCO_2\big|_{thermal}$, reveals that the warming of the sea surface from winter to summer tends to increase surface ocean pCO_2 everywhere, with values reaching as high as nearly 200 μatm (figure 8.3.7b). A comparison of this thermally forced pCO_2 amplitude with the observed pCO_2 amplitude (figure 8.3.7a) shows that this component can explain the sign of the summer-minus-winter change in the subtropical gyres, but tends to overestimate the magnitude. In the high latitudes, the observed sign of the change is opposite to that forced by seasonal SST changes. Here, SST predicts an increase in pCO_2 from winter to summer, whereas the observations clearly show a decrease. This suggests that the effect of the seasonal SST changes on oceanic pCO_2 must be counteracted nearly everywhere by seasonal reductions in pCO_2 induced by changes in *DIC* and *Alk*, i.e., $\Delta pCO_2\big|_{DIC,\,Alk}$. We estimate this component simply by subtracting the thermal component from the observed summer-minus-winter pCO_2 difference, $\Delta pCO_2\big|_{observed}$ i.e.,

$$\Delta pCO_2\big|_{DIC,\,Alk} = \Delta pCO_2\big|_{observed} - \Delta pCO_2\big|_{thermal} \qquad (8.3.26)$$

As shown in figure 8.3.7c, the magnitude of these *DIC*- and/or *Alk*-driven pCO_2 changes is smaller than the thermally driven changes in the subtropical latitudes, while in the high latitudes, the *DIC*- and/or *Alk*-driven changes apparently outweigh the winter-to-summer increase in pCO_2 stemming from the warming of the sea surface. The negative sign of $\Delta pCO_2\big|_{DIC,\,Alk}$ implies a winter-to-summer drawdown in *DIC* or a winter-to-summer increase in *Alk*. How large are these changes?

We can estimate the magnitude of the required summer-minus-winter changes in *DIC* and *Alk*, ΔDIC and ΔAlk, by using the definitions of the buffer and alkalinity factors (equations (8.3.14) and (8.3.15) i.e.,

$$\Delta DIC \approx \frac{DIC}{pCO_2 \cdot \gamma_{DIC}} \Delta pCO_2\big|_{DIC,\,Alk} \qquad (8.3.27)$$

$$\Delta Alk \approx \frac{Alk}{pCO_2 \cdot \gamma_{Alk}} \Delta pCO_2\big|_{DIC,\,Alk} \qquad (8.3.28)$$

Figure 8.3.7c suggests a $\Delta pCO_2\big|_{DIC,\,Alk}$ of 40 to 80 μatm for the northern hemisphere subtropical gyres. Using low-latitude values for the buffer and alkalinity factors from (8.3.18) and (8.3.19), we compute that a winter-to-summer *DIC* decrease of about 20 to 40 μmol kg^{-1} or an *Alk* increase of 30 to 60 μmol kg^{-1} over the same time period would be required to explain the *DIC*- and/or *Alk*-driven winter-to-summer pCO_2 drawdown. In the high northern latitudes of the North Atlantic, $\Delta pCO_2\big|_{DIC,\,Alk}$ is well over 100 μatm. Given typical high-latitude buffer and alkalinity factors, the *DIC* drawdown must be more than 50 μmol kg^{-1}. Alternatively, *Alk* must increase from winter to summer by more than 60 μmol kg^{-1}.

As we will see below, seasonal variations in *Alk* are small, so that most of the $\Delta pCO_2\big|_{DIC,\,Alk}$ variations are, in fact, a result of a seasonal drawdown of *DIC*. But what, then, controls this *DIC* drawdown? Is it air-sea gas exchange, mixing, and/or biology? Since we know the air-sea difference in pCO_2, we can already assess the contribution of air-sea gas exchange. In the high northern latitudes, air-sea gas exchange can be excluded. This is because surface waters in this region are strongly undersaturated with respect to atmospheric CO_2 in summer (figure 3.1.3b), thus taking up CO_2 from the atmosphere. This leads to an increase in *DIC* rather than a decrease as required to explain the winter-summer pCO_2 drop. Therefore, in the high northern latitudes, it must be transport, mixing, and biology that dominate variations in *DIC*. In contrast, air-sea exchange cannot be excluded in subtropical regions, as these waters tend to be supersaturated in summertime (figure 3.1.3b). Therefore, some fraction of the required *DIC* reduction from winter to summer could stem from the loss of CO_2 across the air-sea interface.

We investigate in more detail three regions where different processes dominate seasonal pCO_2 variations. These regions are the subtropical gyres, where seasonal

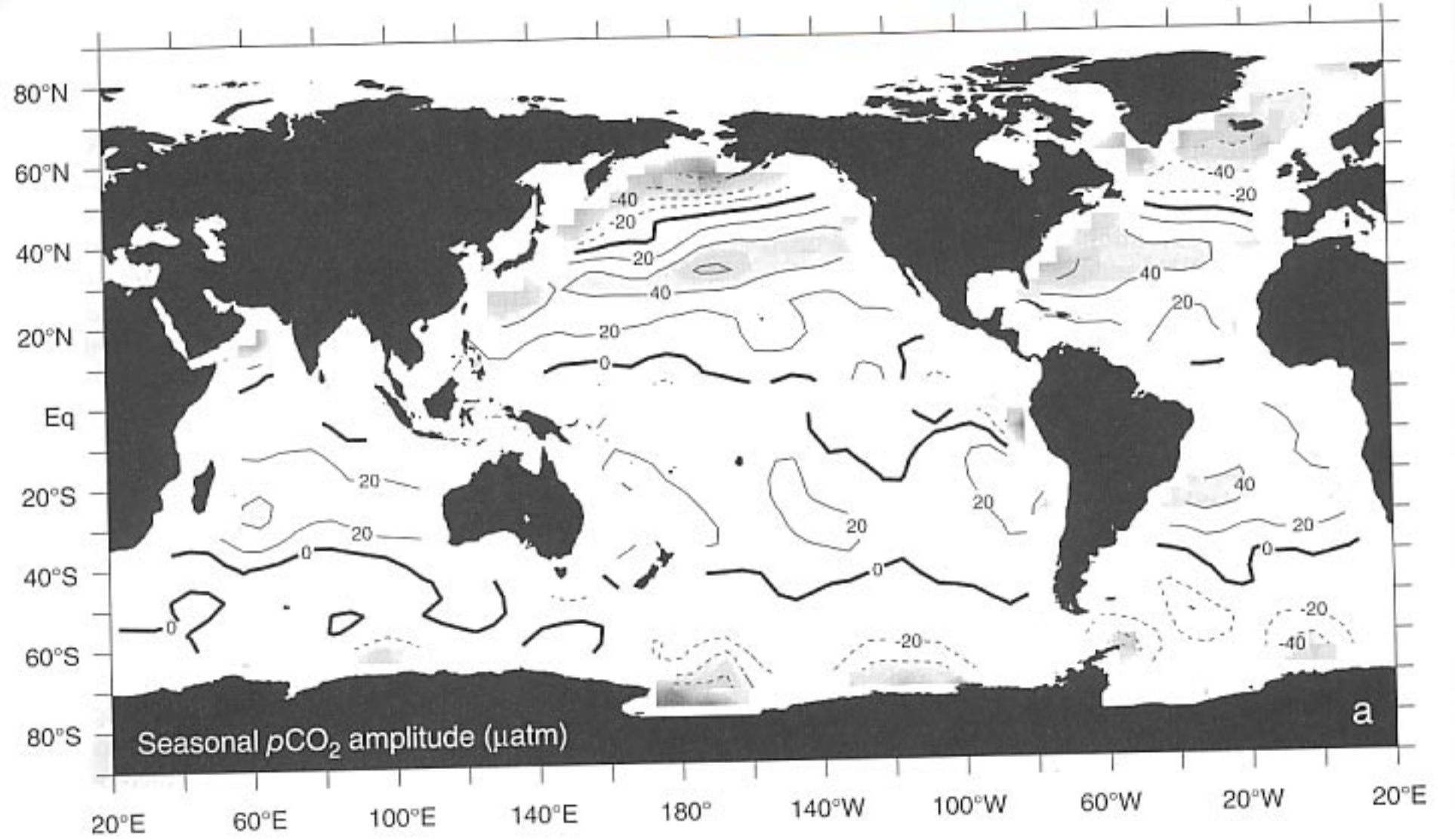

FIGURE 8.3.7: Maps of the seasonal amplitude of surface ocean pCO_2 and its driving forces. (a) summer-minus-winter difference of surface ocean pCO_2. (b) Sea-surface temperature-forced summer-minus-winter difference in surface ocean pCO_2 computed from the temperature sensitivity of pCO_2. (c) *DIC*- and *Alk*-forced summer-minus-winter difference in surface ocean pCO_2, computed by differencing (a) and (b). This change is primarily driven by seasonal variations in biology, and hence can be viewed as the "biological component," but gas exchange and transport/mixing also play a role. In the northern hemisphere, data from the months January through March (JFM) have been averaged to represent winter, and data from the months July through September (JAS) have been averaged for the summer period. In the southern hemisphere, JFM represent the summer season and JAS the winter season. Based on the climatology of *Takahashi et al.* [2002].

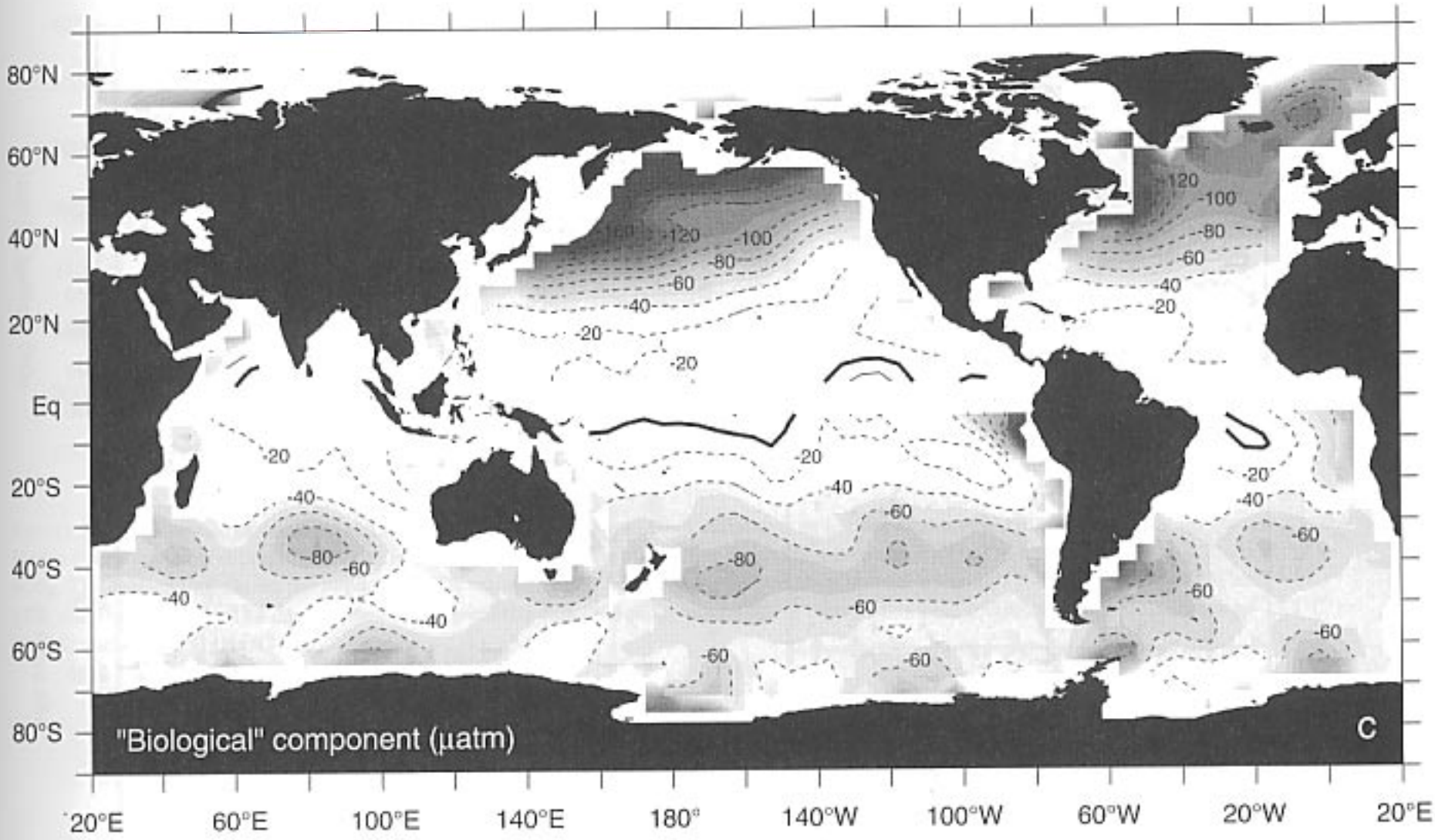

FIGURE 8.3.7: (*Continued*)

pCO_2 changes are primarily temperature controlled, the high latitude North Atlantic, where seasonal pCO_2 changes are dominated by biology and mixing, and the North Pacific, where all three mechanisms are important.

SUBTROPICAL GYRES

Figure 8.3.8 shows seasonally aggregated time series of temperature, *sDIC*, $^{13}C/^{12}C$ ratio of *DIC*, *sAlk*, and oceanic pCO_2 in the surface mixed layer at the Bermuda Atlantic Time-series Study (BATS) site, which lies near Bermuda in the northwestern Sargasso Sea [*Gruber et al.*, 2002]. Figure 8.3.9 shows a similar time series from the Hawaii Ocean Time-series (HOT) site, which is located north of the Hawaiian island chain [*Keeling et al.*, 2004]. Both sites exhibit well-defined seasonal cycles in *sDIC* and pCO_2 (see discussions by *Gruber* [1998], *Bates et al.* [1996b], *Quay and Stutsman* [2003], and *Keeling et al.* [2004]), but negligible variations in *sAlk*, with the exception of a few brief drawdowns occurring at BATS apparently linked to localized blooms of calcifying organisms (most likely coccolithophorids) [*Bates et al.*, 1996a]. The seasonal amplitude of *sDIC* at BATS is about 30 μmol kg^{-1}, approximately twice as large as that observed at HOT and in good agreement with our rough estimates based on (8.3.27).

The competing effects of changing temperature and *sDIC* on the seasonal evolution of pCO_2 at BATS are shown in more detail in figure 8.3.10a. If *sDIC* were kept constant, the seasonal cycle in temperature at this station would lead to a seasonal amplitude of more than 110 μatm, with a maximum occurring in mid-August. If temperature were kept at the annual mean value, the seasonal changes in *sDIC* would lead to a pCO_2 change opposite in phase and with an amplitude of about 60 μatm. The situation is similar but less pronounced in the subtropical North Pacific [*Keeling et al.*, 2004] (figure 8.3.10b). Thus, the detailed time-series data confirm the general trends for the subtropical gyres seen from the global maps very well, i.e., that in these regions, the thermally forced increase in pCO_2, $\Delta pCO_2|_{thermal}$, outweighs the negative $\Delta pCO_2|_{DIC,\,Alk}$ component, leading to a winter-to-summer increase in oceanic pCO_2 as displayed in figure 8.3.7a.

Having established the causes for the seasonal changes in pCO_2, what is driving the seasonal changes in *sDIC*? Of particular interest is the summer/fall period, when *sDIC* is drawn down almost continuously every year at both sites in the absence of measurable nitrate and phosphate concentrations (see also discussion in section 4.3). The processes that we need to consider are air-sea gas exchange (*ex*), net community production (*ncp*), i.e., net primary production minus community respiration, lateral transport (*trsp*), vertical diffusion (*diff*), and vertical entrainment (*ent*). The latter process describes the transport of *DIC* from the thermocline into the mixed layer whenever the surface mixed layer deep-

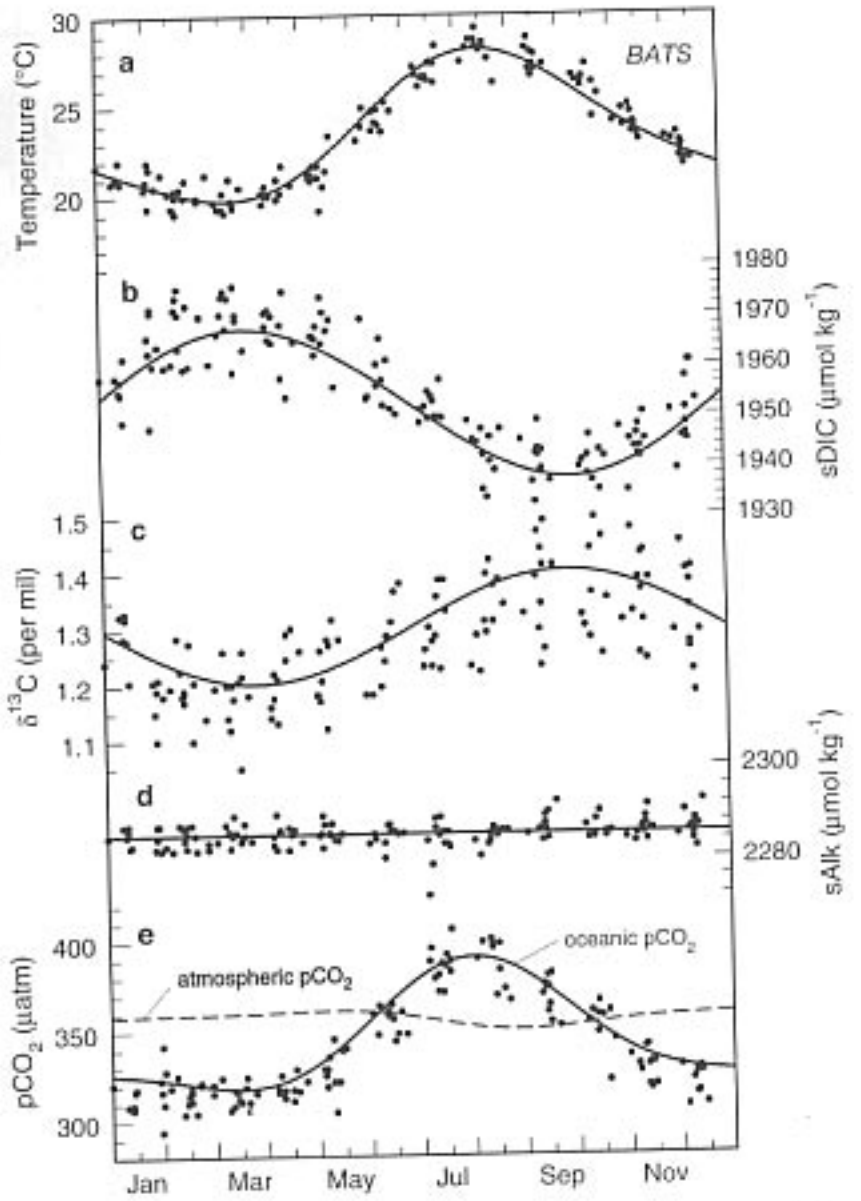

FIGURE 8.3.8: Annual composite time series of upper ocean quantities at the Bermuda Atlantic Time-series Station (BATS) in the subtropical Atlantic (31°50'N, 64°10'W): (a) temperature, (b) salinity-normalized *DIC*, (c) the reduced isotopic ratio ($\delta^{13}C$) of *DIC*, (d) salinity-normalized *Alk*, and (e) computed pCO_2. The filled circles represent the observations, whereas the smooth curve represents the results of a harmonic fit through the observations. Also shown in (e) is the estimated atmospheric pCO_2 near Bermuda. Data are for 1988–2001. Based on data reported by *Gruber et al.* [2002].

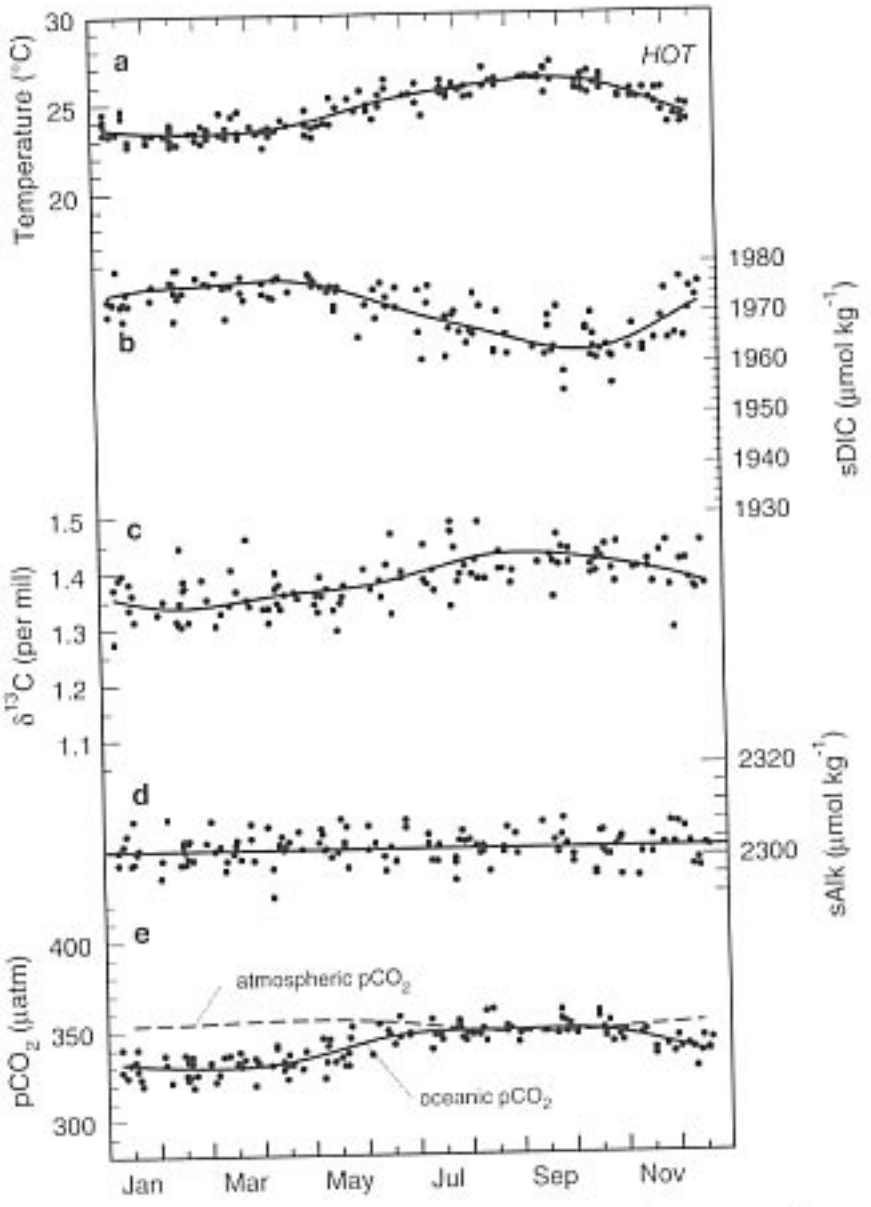

FIGURE 8.3.9: As 8.3.8 except for the Hawaii Ocean Time-series (HOT) ALOHA site in the subtropical North Pacific (22°45'N, 158°00'W). Based on data reported by *Keeling et al.* [2004].

ens. The time-rate of change for the mean *sDIC* concentration in the mixed layer can therefore be written as:

$$\frac{\partial sDIC}{\partial t} = \left.\frac{\partial sDIC}{\partial t}\right|_{ex} + \left.\frac{\partial sDIC}{\partial t}\right|_{ncp} + \left.\frac{\partial sDIC}{\partial t}\right|_{trsp} + \left.\frac{\partial sDIC}{\partial t}\right|_{diff} + \left.\frac{\partial sDIC}{\partial t}\right|_{ent} \qquad (8.3.29)$$

Near Bermuda, air-sea gas exchange can explain a fraction of this drawdown, as oceanic pCO_2 is greater than atmospheric pCO_2 for most of this period (see figure 8.3.8e). However, estimates of the CO_2 evasion during this period are an order of magnitude too small to explain the drawdown [*Michaels et al.*, 1994, *Gruber et al.*, 1998]. Near Hawaii, oceanic pCO_2 is actually undersaturated for most of the year (see figure 8.3.9e), therefore air-sea gas exchange would tend to increase *sDIC* from spring to fall.

Therefore, other processes, either of biological origin or of a physical nature, such as transport and mixing, must create the seasonal reduction in *sDIC*. We learned in chapter 4, on the basis of several lines of evidence, that the *sDIC* drawdown near Bermuda is most likely caused by biology and not by physical processes. One such line of evidence is the concomitant observation of an increase in the $^{13}C/^{12}C$ ratio of *DIC* (figure 8.3.8c). Plants strongly prefer the light isotope ^{12}C over the heavier isotope ^{13}C during the photosynthetic uptake of CO_2, leading to isotopically light organic matter (low $\delta^{13}C$ values), whereas the remaining pool of inorganic carbon becomes isotopically heavier (high $\delta^{13}C$). This biological fractionation is substantially larger than the fractionation by any other process, giving the opportunity to use observations of $\delta^{13}C$ as an indicator of the biological uptake and release of CO_2.

Figure 8.3.11 shows the results of two studies that used the concurrent $^{13}C/^{12}C$ and *DIC* observations as well as other observations to diagnose the relative contribution of the different processes affecting the *sDIC*

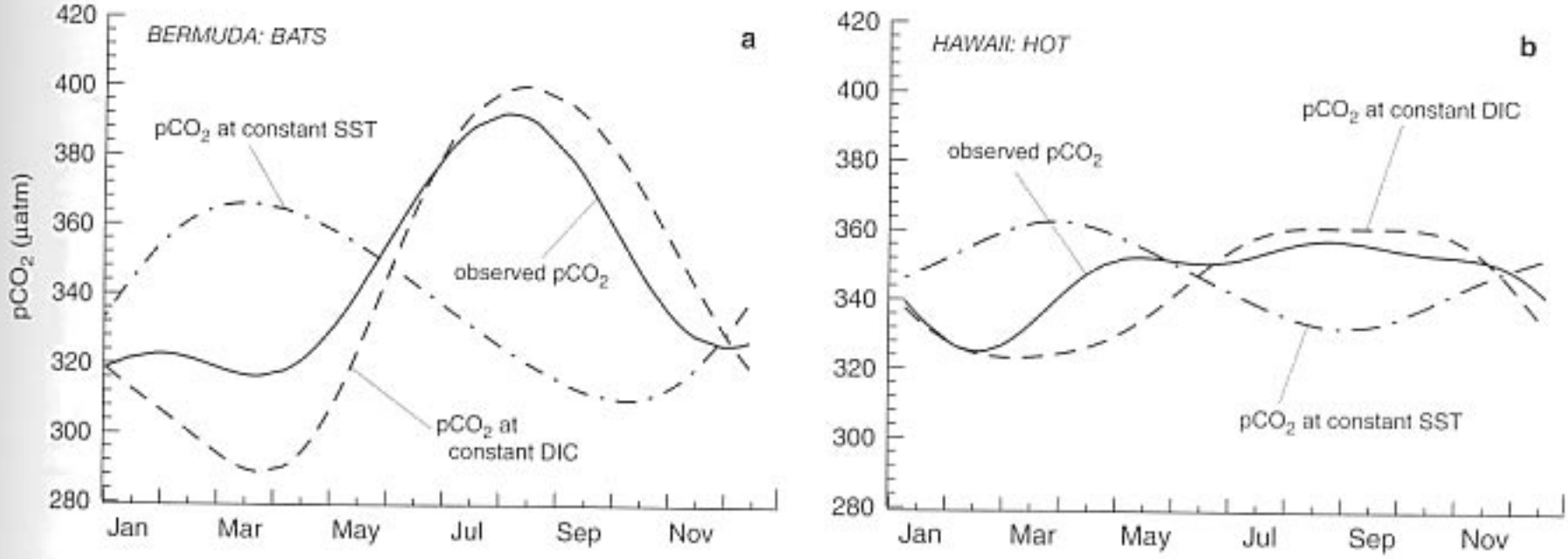

FIGURE 8.3.10: The role of variations in SST and DIC in driving seasonal variations in surface ocean pCO_2 in the subtropical gyres: (a) results for the BATS site, and (b) results for the HOT site. The solid line shows the results of a harmonic fit to the observed seasonal variations of pCO_2. The dashed line shows the expected pCO_2 variations if *sDIC* is held constant at its annual mean of 1954 μmol kg^{-1} (BATS) and 1971 μmol kg^{-1} (HOT). The dash-dotted line depicts the expected pCO_2 variations in case SST is held constant at its annual mean of 23.1°C (BATS) and at 24.8°C (HOT).

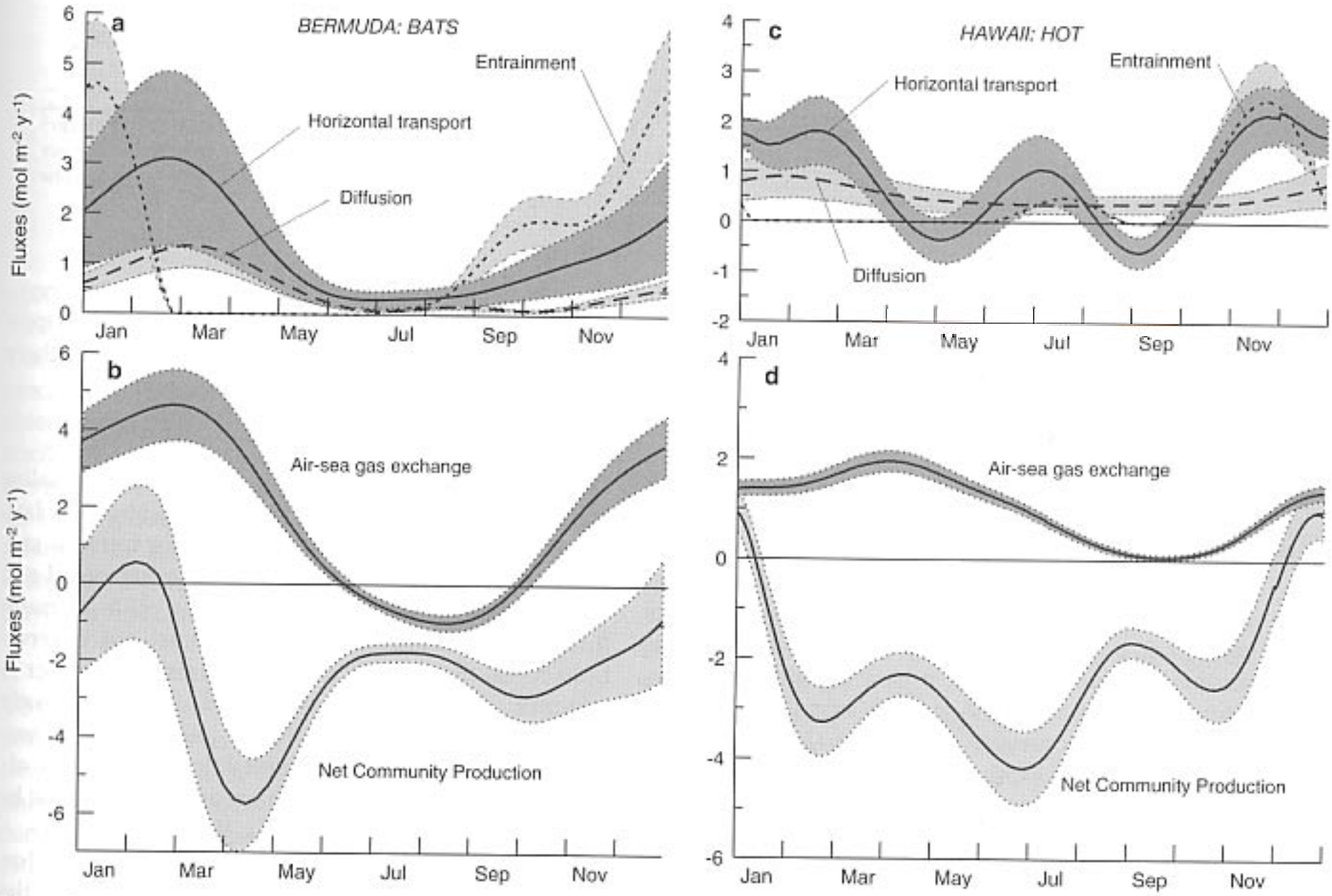

FIGURE 8.3.11: Diagnostically inferred contribution of the processes controlling the seasonal cycle of *sDIC* in the upper ocean cycle at (a–b) BATS and (c–d) HOT. The solid lines denote the computed curve for the standard set of parameters, and the dotted lines denote the upper and lower limit of the uncertainty intervals as evaluated from Monte Carlo simulations. Adapted from *Gruber et al.* [1998] and *Keeling et al.* [2004].

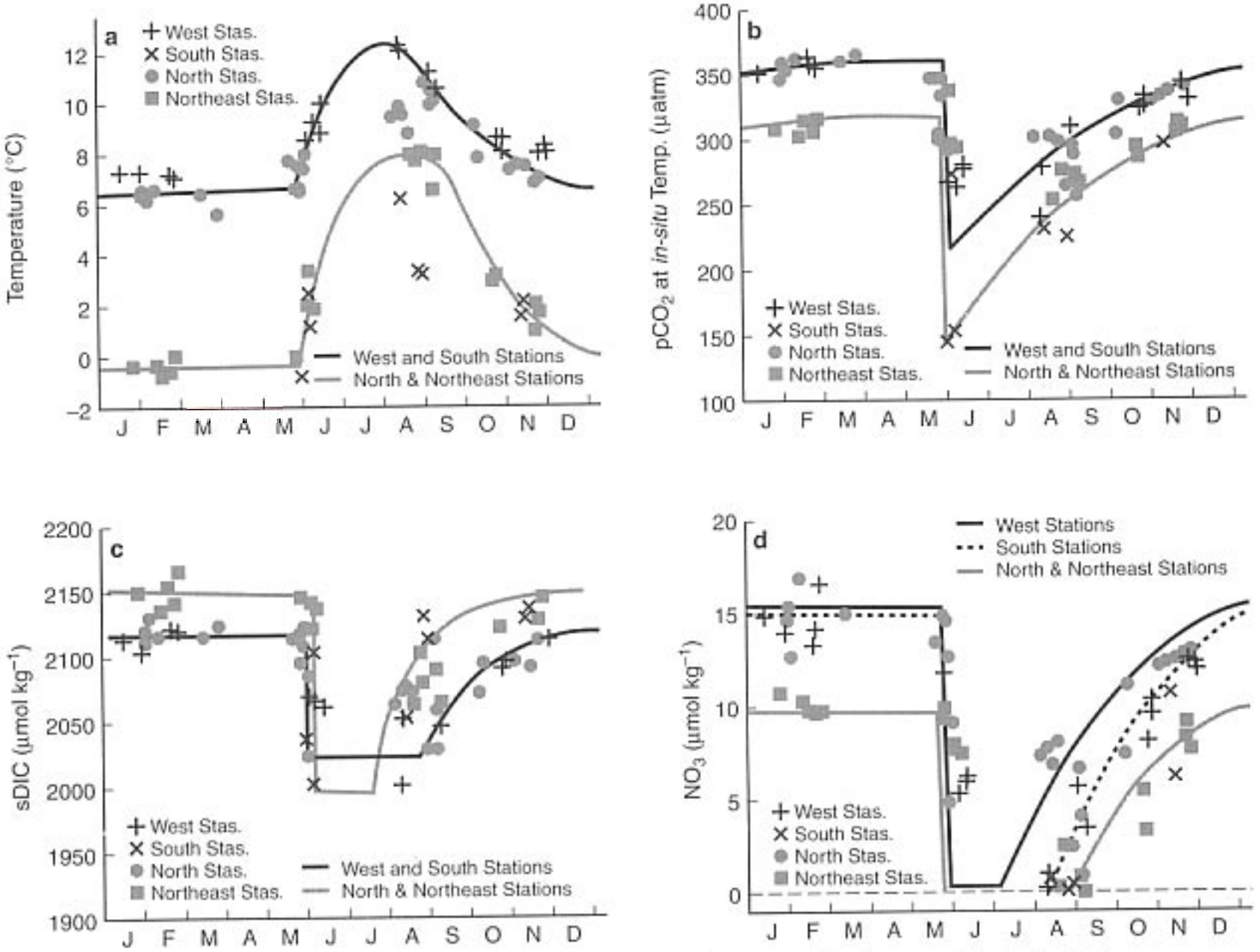

FIGURE 8.3.12: Seasonal observations of upper ocean quantities made at four groups of station around Iceland within approximately 120 miles from shore: (a) surface ocean temperature; (b) pCO_2 in surface water at *in situ* temperature; (c) *sDIC*; (d) nitrate. The curves indicate a general seasonal trend. Adapted from *Takahashi et al.* [1993].

evolution in the mixed layer at BATS and HOT; i.e., they determined each term in (8.3.29) [*Gruber et al.*, 1998, *Keeling et al.*, 2004] (see also studies by *Marchal et al.* [1996], *Bates et al.* [1996b] and *Quay and Stutsman* [2003]). According to these diagnostic analyses, the seasonal cycle of *sDIC* at both locations is a consequence of a complex interplay between the various processes, with different processes dominating at different times of the year. Both studies show also that the spring-to-summer drawdown of *sDIC* at both sites is primarily of biological origin, i.e., a result of net community production. The reasons why biology is able to have a positive net community production in the absence of any measurable nutrients is still somewhat of a mystery. In chapter 4, we suggested that N_2 fixation is the most likely candidate process (see also chapter 5), although we could not provide a satisfactory answer to the problem of where the required phosphorus would come from, particularly not in the case of the North Atlantic, where near-surface concentrations of phosphate are much lower than those of nitrate (see figure 5.1.4 and *Wu et al.* [2000]). Vertical migration has been suggested [*Karl et al.*, 1992], but has not yet been demonstrated to be of quantitative importance. This is a wonderful illustration of how much there is still to learn about ocean biogeochemistry.

NORTH ATLANTIC

The high latitudes of the North Atlantic show smaller winter-to-summer warming than the subtropical latitudes to the south. Nevertheless, if there were no seasonal changes in *DIC* and *Alk*, this warming would still lead to winter-to-summer increases in pCO_2 of more than 40 μatm (figure 8.3.7b). In contrast, the observations reveal that oceanic pCO_2 decreases from winter to summer. Since salinity-normalized alkalinity mostly behaves conservatively without a clearly defined seasonal cycle over the entire North Atlantic [*Brewer et al.*, 1986, *Millero et al.*, 1998], this decrease in pCO_2 must be caused by a sharp reduction of *sDIC*.

Indeed, data from time series stations around Iceland (figure 8.3.12) and from other stations in the North Atlantic reveal precipitous drops of *sDIC* occurring in spring [*Peng et al.*, 1987; *Takahashi et al.*, 1993]. At the Iceland sites, the observed *sDIC* drop of

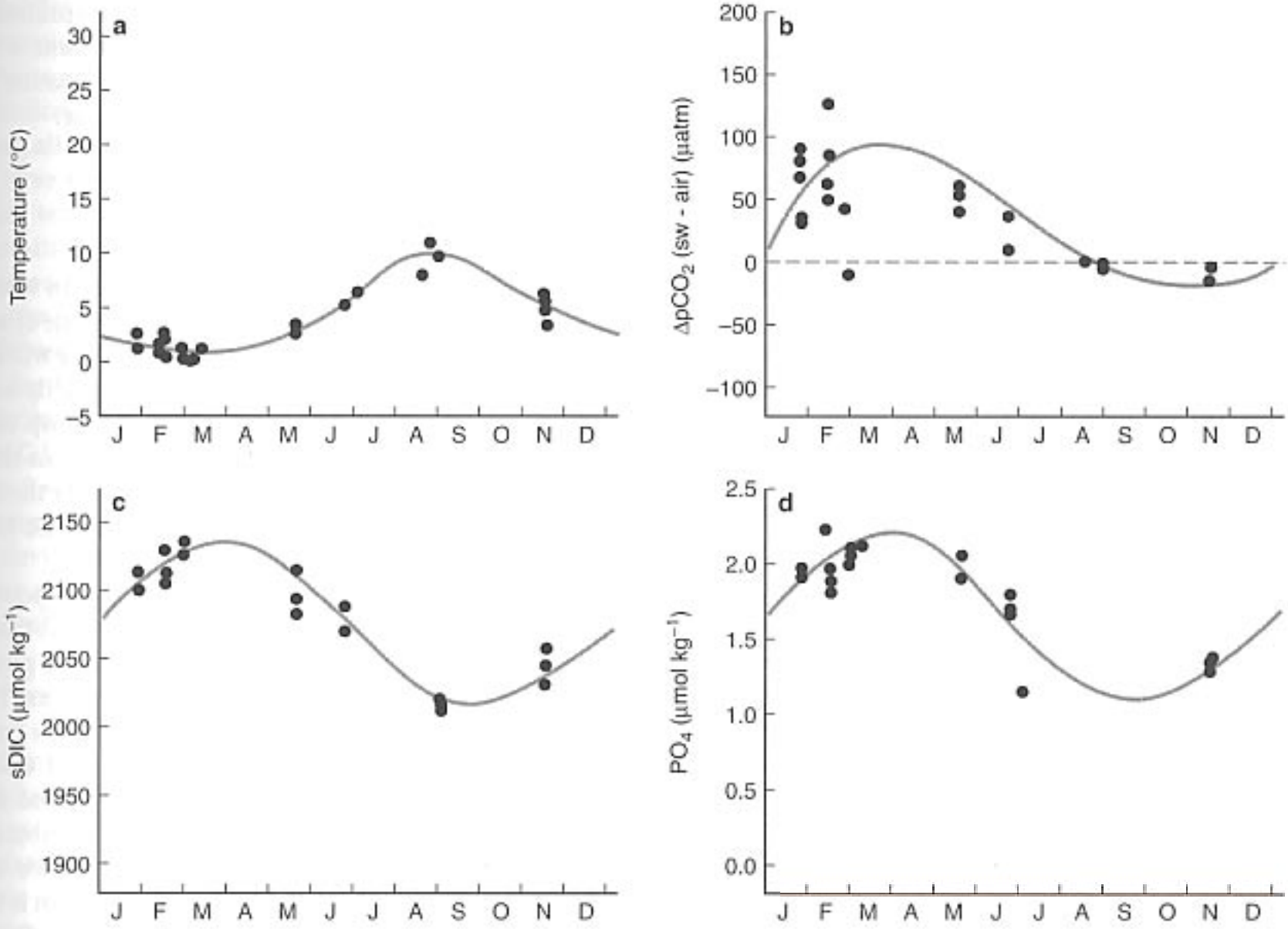

FIGURE 8.3.13: Seasonal changes of (a) temperature, (b) sea-air pCO_2 difference, (c) *sDIC*, and (d) phosphate observed in the surface mixed layer waters of the northwestern subarctic Pacific (50°N–54°N; 162°E–170°E). Circles represent actual observations, while the line was added to emphasize a general seasonal trend. Adapted from *Takahashi et al.* [1993].

>100 µmol kg^{-1} reduces pCO_2 by more than 150 µatm. This is enough to compensate for the warming effect. The drop of *sDIC* in spring is accompanied by equally precipitous nutrient decreases in nearly standard stoichiometric ratios. Thus, the *sDIC* drop likely can be attributed to the phytoplankton spring bloom typical of the northern North Atlantic (see discussion in chapter 4). In conclusion, in the high latitudes of the North Atlantic, the seasonal changes of *sDIC* and pCO_2 are dominated by biological processes, with temperature playing a lesser role.

North Pacific

Seasonal changes in SST are somewhat larger in the North Pacific than in the North Atlantic, largely because North Atlantic SSTs do not get as cold in winter due to the large northward heat transport in this basin. This leads to a stronger winter-summer thermal forcing on pCO_2, with values reaching well above 100 µatm (figure 8.3.7b) across a wide swath of the high-latitude North Pacific. Nevertheless, as was the case in the high-latitude North Atlantic, the surface ocean warming from winter to summer is accompanied by a reduction in surface ocean pCO_2.

Figure 8.3.13 shows the seasonal evolution of the upper ocean carbon cycle in the northwestern subarctic Pacific in more detail (region from 50°N to 54°N, 162°E to 170°E). Here, pCO_2 and the concentrations of *sDIC* and nutrients are highest in winter and lowest during summer. *Takahashi et al.* [1993] attributed this to upwelling and entrainment of deep waters during winter and biological uptake in summer. Therefore, as in the North Atlantic, the *sDIC* reduction by biological uptake in spring and summer is large enough to outweigh the warming effect on pCO_2.

It is intriguing to compare the seasonal pattern of *sDIC* in the subarctic North Pacific with that in the northern North Atlantic. The precipitous drop in *sDIC* and nutrients observed in springtime in the northern North Atlantic is absent in the subarctic Pacific. Why is this the case? Since we attributed the observed drawdowns in both regions to the biological uptake of *sDIC*, these differences must be caused by differences in the seasonal evolution of phytoplankton activity. We have seen in chapter 4 that the North Atlantic supports a

large spring bloom, whereas the development of such a bloom is strongly attenuated in the North Pacific (see figure 4.3.14) for reasons not completely understood. We have mentioned zooplankton grazing and iron limitation as the two main hypotheses, with evidence accumulating that iron is the lead cause. This thus represents a remarkable example of the impact of iron limitation of phytoplankton on the upper ocean carbon cycle.

8.4 Water Column

We learned in the introduction that the surface concentration of *sDIC* is lower than the deep ocean concentration by about 15% (figure 8.1.2). This vertical gradient has major consequences for atmospheric carbon dioxide. If the ocean were to be mixed uniformly, models show that atmospheric CO_2 would climb by more than 50% as previously noted. It is thus of considerable importance to understand what "gradient makers" act to maintain the *sDIC* gradient in the face of ocean circulation and mixing, which are continuously trying to weaken and alter these gradients.

We have identified two biological processes that contribute toward creating the vertical gradient of *sDIC*: the *soft-tissue pump* and the *carbonate pump*. We have also seen that air-sea gas exchange, responding to changes in surface ocean pCO_2, which in turn are driven by changes in temperature, *DIC*, and *Alk* variations, can also lead to variations in oceanic *sDIC*. We will refer to this process as the *gas exchange pump*, although the word "pump" is not really appropriate here, since this process acts only in the surface ocean. It is, in fact, ocean circulation and mixing that takes these gas exchange–induced surface ocean variations and transports/mixes them into the ocean interior, leading then to vertical gradients in *sDIC*. Note that our definition of the *gas exchange pump* is different from the classical definition of the *solubility pump* by *Volk and Hoffert* [1985]. As we will demonstrate below, the solubility pump is a component of the gas exchange pump.

We expect on the basis of the strong covariation between *sDIC* and phosphate (figure 8.1.4a) that the soft-tissue pump likely plays a major role. However, figure 8.1.4b also reveals that variations in *sDIC* roughly track a trend versus temperature that is expected from the temperature sensitivity of the equilibrium *sDIC* concentration for a constant atmospheric CO_2 concentration. Clearly, both processes, soft-tissue pump and temperature variations driving the gas exchange pump, could by themselves explain the majority of the *sDIC* variations, but they cannot do so simultaneously. Which one is dominating, and what is the role of the third process, i.e., the carbonate pump?

Outline

We will tackle this question by breaking the *sDIC* observations down into individual components that can be identified with the three different pumps. We introduce this breakdown by going through a sequence in which we separately consider the distribution if only one or two of these processes are simultaneously active. We will see that we can associate the soft-tissue pump directly with variations in phosphate, and the carbonate pump with variations in nitrate-corrected alkalinity, giving us then the gas exchange component as a residual from the observed *sDIC* distribution once the anthropogenic CO_2 component has been subtracted.

We then discuss the distribution of each component in turn, noting that the distribution of the soft-tissue pump harbors few suprises, while the carbonate pump component reveals some interesting new features. The most interesting component is the gas exchange component, which shows a completely unexpected distribution. We attempt to unravel the reasons behind this puzzling pattern, first looking at the global distribution only, and then analyzing regional differences. We will see that the key to understanding this distribution is the fact that heating- and cooling-induced air-sea CO_2 fluxes and biologically induced air-sea CO_2 fluxes often oppose each other. The resulting CO_2 flux pattern is further modified by the relatively long timescale of air-sea exchange of CO_2, so that surface waters are seldom in equilibrium with atmospheric CO_2. This causes a substantial difference between the "potential" gas exchange pump, i.e., the oceanic *sDIC* pattern that would exist if surface waters were fully equilibrated, and the actually observed gas exchange pump. In section 8.5, we connect the ocean interior distribution of the gas exchange component with surface fluxes, permitting us to investigate in greater detail the consequences of the opposing trends of heat fluxes and biology on the gas exchange pump and how kinetic limitations alter the flux pattern.

Pump Components

We start our pump separation with a thought experiment using a two-dimensional, i.e., latitude-depth model of the ocean, but focus on the mean vertical gradient of *sDIC* only. We then use the insights from this thought experiment to define the pump components more rigorously. The approach we follow here is explained in more detail in *Gruber and Sarmiento* [2002].

Our first experiment considers an ocean that has no gas exchange and no biology, but a realistic temperature distribution. As the inhibition of air-sea gas exchange prevents the expression of the temperature-dependent

solubility, such an ocean would have uniform *DIC* concentration, except for small variations induced by the addition or removal of freshwater (figure 8.4.1a). These latter variations are largely eliminated by our using salinity-normalized *DIC* for our analysis.

If we make the ocean isothermal, i.e., let it have constant temperature, and add biology to it, while still not permitting air-sea gas exchange to occur, *sDIC* will begin to show variations. In a case where we just have organic matter production by phytoplankton in the upper ocean followed by export and remineralization of this material at depth, *sDIC* would be directly proportional to the distribution of phosphate, with a slope that is equal to the C:P stoichiometric ratio of organic matter, $r_{C:P}$ (figure 8.4.1d). We can therefore identify the soft-tissue pump in the absence of gas exchange, ΔC_{soft}, by looking at deviations of phosphate relative to a constant reference value, $[PO_4^{3-}]^{ref}$, which we set equal to the mean phosphate concentration in the surface ocean:

$$\Delta C_{soft} = r_{C:P} \cdot ([PO_4^{3-}] - [PO_4^{3-}]^{ref}) \tag{8.4.1}$$

Similarly, if the formation and dissolution of biogenic calcium carbonate were the only process affecting *DIC* in an isothermal ocean without air-sea gas exchange, variations of *sDIC* would be coupled entirely to variations in *sAlk*, with a slope of 1:2 (figure 8.4.1g). We can thus identify the contribution of the carbonate pump in the absence of gas exchange, ΔC_{carb}, by studying deviations of *sAlk* relative to a constant background value, $sAlk^{ref}$, chosen here to be the global mean *sAlk* in the surface ocean. In the real ocean, *sAlk* is also affected by the soft-tissue pump, and we therefore have to add a small correction that is proportional to nitrate:

$$\Delta C_{carb} = \frac{1}{2}(sAlk - sAlk^{ref} + [NO_3^-] - [NO_3^-]^{ref}) \tag{8.4.2}$$

$$= \frac{1}{2}(sAlk - sAlk^{ref} + r_{N:P} \cdot ([PO_4^{3-}] - [PO_4^{3-}]^{ref})) \tag{8.4.3}$$

where we made use of the very tight coupling between the cycling of nitrate and phosphate (see discussion in chapter 5) to write our separation in terms of phosphate only. Therefore, the term $r_{N:P} \cdot ([PO_4^{3-}] - [PO_4^{3-}]^{ref})$ accounts for the impact of the soft-tissue pump on *Alk*. The sign of this correction term is positive, since the remineralization of organic matter decreases *Alk*. *Brewer et al.* [1975] introduced the term "potential alkalinity" for this nitrate corrected alkalinity, i.e., $P_{Alk} = Alk + NO_3^-$. Therefore, except for the salinity normalization, ΔC_{carb} is equal to the difference between observed P_{Alk} and a constant reference P_{Alk}^{ref}.

Now, let us permit gas exchange with the atmosphere to occur. In our first case of an abiological ocean, the exchange of CO_2 across the air-sea interface permits the inorganic CO_2 system in the surface ocean to work toward an equilibrium with atmospheric CO_2. As a result, waters that cool as they are transported into higher latitudes will tend to take up CO_2 from the atmosphere, thereby getting enriched in *sDIC*. Waters that warm up as they are transported in the opposite direction lose CO_2 and consequently have lower *sDIC* concentrations. As the high latitudes constitute the source regions for the deep ocean, a vertical gradient of *sDIC* will develop (figure 8.4.1b). The magnitude of this vertical gradient depends on how rapidly air-sea gas exchange can supply the CO_2 necessary to bring high-latitude surface waters that sink into the abyss close to saturation (figure 8.4.1c).

The effect of air-sea gas exchange on the *sDIC* distribution in an isothermal, biological ocean is opposite to that in the abiological ocean discussed above (except for the small carbonate pump effect discussed later; figure 8.4.1e). Gas exchange will tend to remove carbon from the high-latitude outcrops of the carbon-rich deep waters, and add it to the lower-latitude surface waters [*Gruber and Sarmiento*, 2002; *Toggweiler et al.*, 2003]. As a result, the vertical gradient of *sDIC* produced by biological processes will be reduced in the presence of air-sea exchange. Again, the magnitude of this reduction in the gradient depends on how fast air-sea exchange is removing CO_2 from the surface relative to the removal by other processes, such as biological uptake (figure 8.4.1f).

Thus, the impact of air-sea exchange on the distribution of *sDIC* is twofold and includes a thermally driven as well as a biologically driven component. We refer to the sum of these two effects as the *gas exchange pump*:

$$\Delta C_{gas\ ex} = \Delta C_{gas\ ex}^{bio} + \Delta C_{gas\ ex}^{therm} \tag{8.4.4}$$

Note that the commonly used term "solubility pump" [*Volk and Hoffert*, 1985] refers only to the thermal component of the gas exchange pump, i.e., $\Delta C_{gas\ ex}^{therm}$, i.e. those variations in *sDIC* that are driven only by temperature variations and ocean transport and mixing. Unfortunately, the gas exchange pump cannot be estimated directly from observations. Therefore, we estimate this pump by subtracting the two biological pumps from the observations, while taking into account that the invasion of anthropogenic CO_2 from the atmosphere has already altered the upper ocean distribution of *sDIC*. We have developed the means to estimate this contribution, C_{ant}, directly from observations [*Gruber et al.*, 1996] (see chapter 10), and subtract it from the observed *sDIC* distribution to reconstruct a preindustrial *sDIC* distribution. We thus estimate $\Delta C_{gas\ ex}$ by

$$\Delta C_{gas\ ex} = sDIC - sDIC^{ref} - C_{ant} - \Delta C_{soft} - \Delta C_{carb} \tag{8.4.5}$$

where DIC^{ref} is a constant reference concentration chosen here as the mean surface ocean *sDIC* in preindustrial times. Note that this reference concentration and those used in the definitions of ΔC_{soft} and ΔC_{carb}

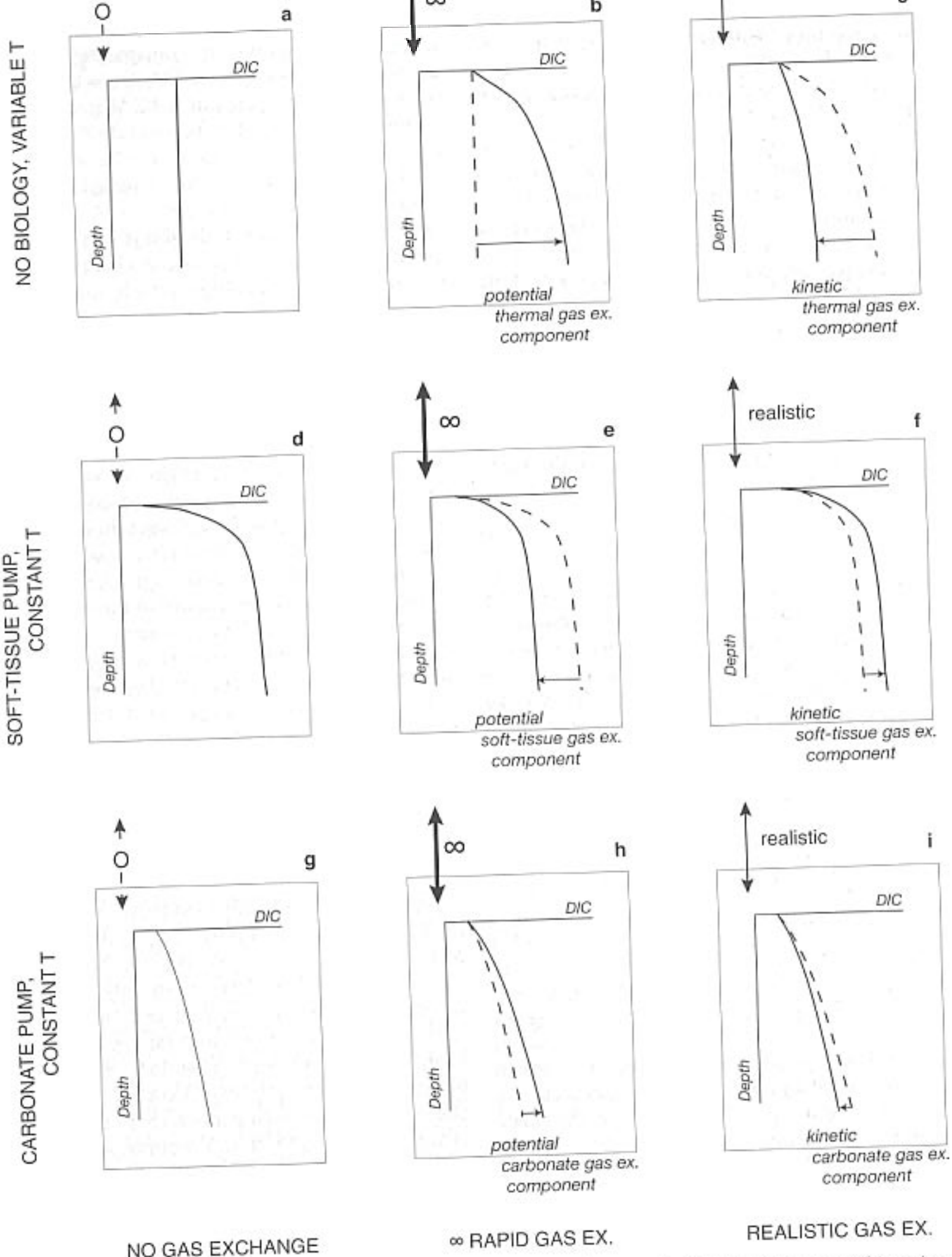

FIGURE 8.4.1: Hypothetical vertical profiles of *sDIC* in a series of thought experiments to elucidate the contributions of the various pump components. The first row depicts the *sDIC* distribution in an abiological ocean with realistic temperature distribution and various gas exchange scenarios. The second row shows the *sDIC* distributions in a biological ocean with just the soft-tissue pump operating and with fixed temperature distribution under various gas exchange scenarios. The third row is as the second, but with only the carbonate pump being active. The potential gas exchange pump components are the changes in the *sDIC* distributions that occur when one goes from an ocean without air-sea gas exchange to one with infinitely fast gas exchange. The kinetic gas exchange components are then the changes in *sDIC* that are caused by replacing the infinitely fast gas exchange with a realistic one. The main point to note is that the thermal and biological gas exchange pump components have a tendency to operate in opposite directions. This is the main reason why the gas exchange pump component is relatively small.

were only added for the convenience of setting the global mean surface concentration of each of the three pump components to zero. This is an arbitrary choice and has no influence on the interpretation, since the information of interest is contained in the gradients of these pump components from one place to another.

It needs to be emphasized that ΔC_{soft} and ΔC_{carb} refer only to the impact of ocean biology on *sDIC* in the absence of air-sea gas exchange. Therefore, these two components can be viewed as "potential" pumps. They differ from the common definition of these biological pumps, as the latter include also the impact of biology on the air-sea gas exchange component, i.e., $\Delta C^{bio}_{gas\ ex}$ [*Volk and Hoffert*, 1985; *Toggweiler et al.*, 2003a, b]. If we were able to estimate $\Delta C^{bio}_{gas\ ex}$, we could add it to ΔC_{soft} and ΔC_{carb} and determine the complete contribution of these two processes. However, this is unfortunately not possible on the basis of observations. Below, we will use model results to undertake this split of $\Delta C_{gas\ ex}$ and discuss the implications. Another argument in favor of the pump separation adopted here is that it clearly separates the influence of air-sea gas exchange from the influence of processes that only redistribute *sDIC* internally within the ocean. This can be thought of as separating the closed system response (no exchange with the atmosphere) from the open system response (including exchange with the atmosphere) to processes that lead to perturbation in the oceanic carbon cycle.

We will now discuss the contribution of each of these pumps to the observed distribution of *sDIC* in turn, beginning with the soft-tissue pump. The major focus of the discussion will be on the contribution of the gas exchange pump to the *sDIC* distribution, which holds interesting surprises.

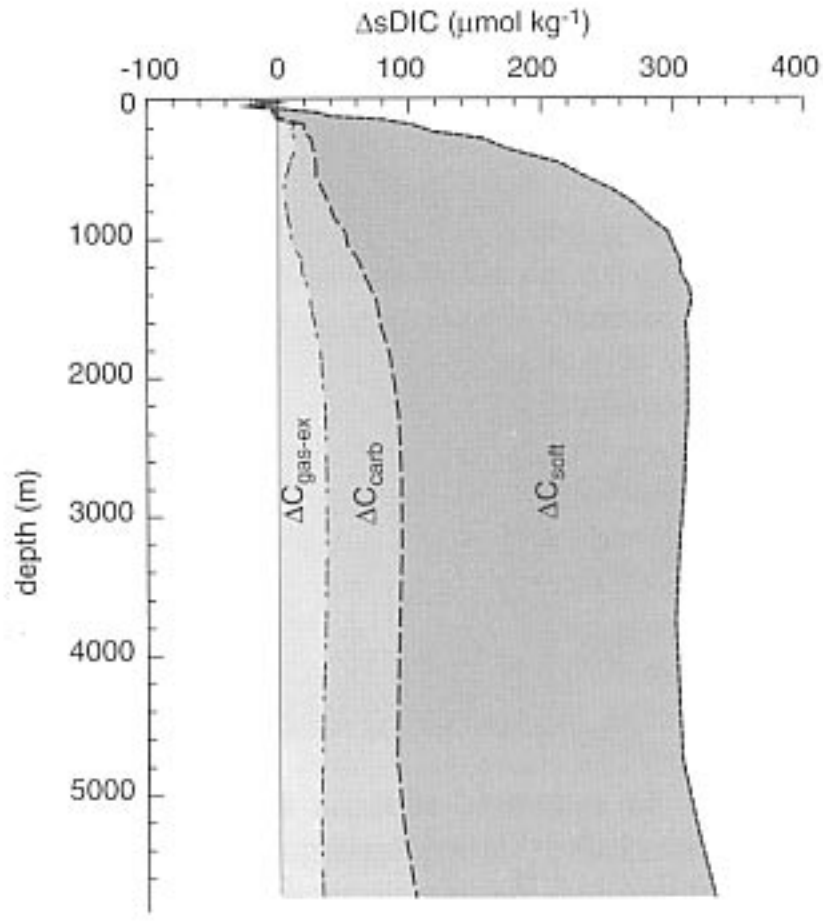

FIGURE 8.4.2: Global mean profiles of the three main carbon pumps. The data are plotted cumulatively. Based on GLODAP data [*Key et al.*, 1994].

The Biological Pumps

Figure 8.4.2 reveals that the soft-tissue pump in the absence of air-sea exchange, ΔC_{soft}, is responsible for about 215 μmol kg^{-1} (70%) of the surface-to-deep gradient of preindustrial *sDIC* of about 305 μmol kg^{-1}. The carbonate pump, ΔC_{carb}, accounts for approximately 60 μmol kg^{-1} (20%) of the observed gradient, and the gas exchange pump, $\Delta C_{gas\ ex}$, for the remainder.

The dominance of the soft-tissue pump in creating the vertical gradient in preindustrial *sDIC* is not surprising, since we have seen this dominance already expressed in the strong covariation between *sDIC* and phosphate (figure 8.1.4a). The substantially smaller contribution of the carbonate pump will be confirmed in chapter 9, where we will show that the downward transport of carbon as $CaCO_3$ is about 10 times smaller than the downward transport of organic matter [*Sarmiento et al.*, 2002]. Figures 8.4.3a and b show the contribution of the biological pumps in the different ocean basins. Again, the soft-tissue and carbonate pump contributions exhibit the expected pattern of increasing contributions of these pumps in the deep waters along the flow path of the lower limb of the global-scale overturning circulation (figure 2.4.11).

A more detailed inspection of figure 8.4.3 reveals that the two biological pumps have quite different vertical structures. Almost the entire surface-to-deep gradient in the soft-tissue component, ΔC_{soft}, occurs in the main thermocline, with little additional contribution below 1000 m. By contrast, the contribution of the carbonate pump component, ΔC_{carb}, to the variability of preindustrial *sDIC* in the main thermocline is relatively small (<40 μmol kg^{-1}). However, ΔC_{carb} increases slowly with depth below 1000 m and reaches a maximum at depths between 2000 to 6000 m. This is significantly deeper than the maximum of ΔC_{soft}, which occurs at about 1000 m.

The difference between ΔC_{soft} and ΔC_{carb} is particularly striking in the Atlantic basin, where ΔC_{carb} gradually increases all the way to the bottom, whereas ΔC_{soft} shows a pronounced maximum in intermediate waters at around 1000 m. The maximum in ΔC_{carb} shoals from the Atlantic to the Indian and Pacific Oceans but still occurs significantly deeper than the maximum in ΔC_{soft}. This indicates that the formation and dissolution of calcium carbonate is a process independent from the formation and remineralization of organic matter. We will discuss the cycling of calcium carbonate in more detail in the following chapter, but we can point out here already that the spatial distribution of ΔC_{carb} is

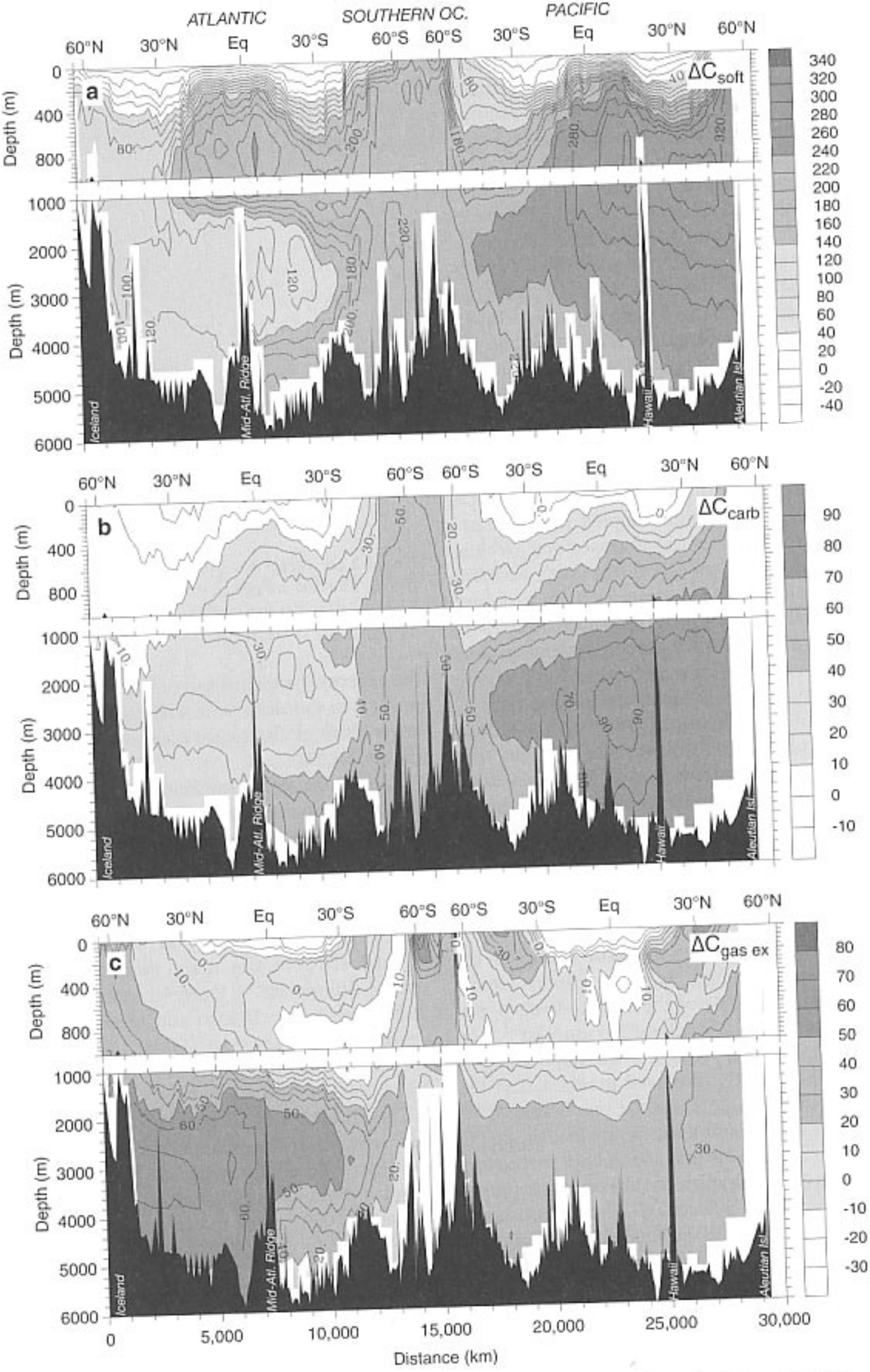

FIGURE 8.4.3: Vertical sections of (a) ΔC_{soft}, (b) ΔC_{carb}, and (c) $\Delta C_{gas\ ex}$, all in units of μmol kg^{-1} along the track shown in figure 2.3.3a. See also color plate 8.

consistent with the variation of the saturation horizons for the two major phases of calcium carbonate, calcite and aragonite. The saturation horizon for aragonite, the more soluble phase, occurs in the Atlantic at depths of about 3000 m, whereas it lies within the main thermocline in the Pacific and Indian Ocean [*Takahashi et al.*, 1981, *Broecker and Peng*, 1982, *Feely et al.*, 2002, *Chung et al.*, 2003].

The Gas Exchange Pump

Let us turn now to the gas exchange pump. Figure 8.4.2 reveals that the contribution of the gas exchange pump to the global mean vertical profile of preindustrial *sDIC* amounts to only about 30 μmol kg^{-1} (10%). How does this compare to what one would expect on the basis of the surface-to-deep temperature gradient? We can estimate this temperature-induced gradient by combining the temperature sensitivity of pCO_2 (8.3.4) with the definition of the buffer factor (8.3.14) (see equation (10.2.31)). This gives, on average, a temperature sensitivity of *DIC* of about 8 to 9 μmol kg^{-1} per degree of temperature change (see slope in figure 8.1.4b). Therefore, with a surface-to-deep temperature gradient of about 18°C, one would expect a temperature-induced surface-to-deep gradient in *sDIC* of about 140 to 160 μmol kg^{-1}. This is several times larger than our estimate on the basis of $\Delta C_{gas\ ex}$. Such a small imprint of air-sea gas exchange on the distribution of *sDIC* is particularly surprising given the strong correlation of *sDIC* with temperature (figure 8.1.4b). Why is this case? Is this small $\Delta C_{gas\ ex}$ signal a result of the biological contribution, $\Delta C^{bio}_{gas\ ex}$, offsetting the thermal component, $\Delta C^{therm}_{gas\ ex}$, or is it because of kinetic limitations, i.e., the slow exchange of CO_2 not permitting the full temperature variations in the ocean to be reflected in *sDIC*?

Consideration of $\Delta C_{gas\ ex}$ in the different ocean basins reveals additional puzzles (figure 8.4.3c). Hidden in the small global mean surface-to-deep difference of $\Delta C_{gas\ ex}$, we find a very large imprint of the gas exchange pump in the deep Atlantic. This indicates that these waters must have taken up a substantial amount of CO_2 from the atmosphere before they descended into the deep Atlantic. The deep Pacific and deep Indian have smaller and vertically more uniform values of $\Delta C_{gas\ ex}$. Figure 8.4.3c also shows that Antarctic Intermediate Water (AAIW), which dominates the deeper thermocline in the southern hemisphere (see salinity minimum in figure 2.4.1), has comparatively low concentrations of $\Delta C_{gas\ ex}$, suggesting that the source waters for AAIW have lost CO_2 to the atmosphere before they descended into the ocean's interior. What are the reasons for these spatial variations in $\Delta C_{gas\ ex}$, and why does the deep Atlantic have such high concentrations of $\Delta C_{gas\ ex}$ in comparison to the deep Indian and Pacific?

The latter question is linked to an important research topic in global carbon cycle research. Since deep waters in the Atlantic flow southward, these high concentrations of $\Delta C_{gas\ ex}$ provide a conduit for transporting CO_2 taken up by the ocean in the northern hemisphere into the southern hemisphere, where it is released back into the atmosphere. In a preindustrial steady-state, such an oceanic southward transport of CO_2 must have been compensated by a northward transport of CO_2 in the atmosphere. This requires the existence in preindustrial times of a south-to-north concentration gradient in atmospheric CO_2. Accurate knowledge of such a preindustrial interhemispheric gradient in atmospheric CO_2 is of prime importance for atmospheric inverse studies that attempt to determine the present sources and sinks of anthropogenic CO_2 in the global carbon cycle [*Keeling et al.*, 1989; *Tans et al.*, 1990; *Ciais et al.*, 1995; *Fan et al.*, 1998; *Gurney et al.*, 2002; *Gloor et al.*, 2003]. This is because one requires accurate estimates of all natural processes causing atmospheric CO_2 variations, before the inversions can determine where anthropogenic CO_2 is taken up currently at the surface of the Earth.

We continue our discussion of the $\Delta C_{gas\ ex}$ distribution by addressing next the puzzle of the small global mean contribution of the gas exchange pump, and consider the Atlantic gas exchange signal afterwards. As we will see, however, the underlying cause for these two patterns is the same. It is the interaction of air-sea fluxes of heat with ocean biology and large-scale ocean circulation that determines how strongly the gas exchange pump influences the oceanic *sDIC* concentrations.

Global Mean

The first key to understanding variations in $\Delta C_{gas\ ex}$ is to recall that both heat fluxes and biological processes control the exchange of CO_2 across the air-sea interface (see (8.4.4)). The second key is that the exchange of CO_2 across the air-sea interface is slow relative to the residence time of waters near the surface. This prevents full expression of the impact of both heat fluxes and biological changes on the respective gas exchange fluxes.

It is therefore instructive to separate the gas exchange pump even further into potential components ($\Delta C^{bio,\,pot}_{gas\ ex}$, $\Delta C^{therm,\,pot}_{gas\ ex}$) that would reflect the $\Delta C_{gas\ ex}$ distribution if gas exchange were infinitely rapid, and into kinetic components ($\Delta C^{bio,\,kin}_{gas\ ex}$, $\Delta C^{therm,\,kin}_{gas\ ex}$) that describe the changes from an infinitely rapid exchange to a case with realistic air-sea gas exchange:

$$\Delta C^{bio}_{gas\ ex} = \Delta C^{bio,\,pot}_{gas\ ex} + \Delta C^{bio,\,kin}_{gas\ ex} \tag{8.4.6}$$

$$\Delta C^{therm}_{gas\ ex} = \Delta C^{therm,\,pot}_{gas\ ex} + \Delta C^{therm,\,kin}_{gas\ ex} \tag{8.4.7}$$

The role of each of these four gas exchange components can be understood better by returning to the thought experiments we introduced at the beginning of

this section to separate ΔC_{soft}, ΔC_{carb}, and $\Delta C_{gas\ ex}$ (see figure 8.4.1). At the same time, we will attempt to estimate the magnitude of each of these components, using a combination of observations and model results.

We start again with an ocean with a realistic temperature distribution, but without biology. We have seen that without air-sea gas exchange, this ocean would have a uniform *sDIC* distribution. We then turn on infinitely rapid air-sea exchange and let the ocean fully equilibrate with a fixed atmospheric pCO_2 of 280 μatm (figure 8.4.1b). The difference between this case and the no-gas-exchange case is the contribution of the potential $\Delta C^{therm}_{gas\ ex}$ pump (also called "potential solubility pump" [*Murnane et al.*, 1999]). The potential $\Delta C^{therm}_{gas\ ex}$ component can be estimated directly from data by computing the *sDIC* concentration in equilibrium with a preindustrial atmospheric pCO_2 of 280 μatm and assuming constant salinity-normalized total alkalinity. The resulting mean global surface-to-deep gradient of $\Delta C^{therm,\ pot}_{gas\ ex}$ amounts to about 155 μmol kg^{-1} (figure 8.4.4).

What happens if we then scale down air-sea gas exchange to realistic values? As it takes about 6 months to equilibrate *DIC* in a 40 m-deep surface layer with the atmosphere (see discussion in section 8.3 above), and typical residence times of surface waters are between a few days to a few years, the CO_2 system in surface waters generally does not achieve equilibration with the atmosphere. Therefore, the potential thermal gas exchange pump cannot be achieved fully (figure 8.4.1), resulting in a reduced vertical *sDIC* gradient (figure 8.4.4), with the difference being the kinetic $\Delta C^{therm}_{gas\ ex}$ effect. Unfortunately, we cannot estimate the kinetic $\Delta C^{therm}_{gas\ ex}$ component directly from observations, but simulations by *Murnane et al.* [1999] indicate that the slow kinetics of CO_2 exchange reduces $\Delta C^{therm}_{gas\ ex}$ by 90 μmol kg^{-1} (see figure 8.4.4), suggesting that the slow kinetics of air-sea gas exchange plays an important role. *Toggweiler et al.* [2003] pointed out, however, that this particular model may tend to overestimate the kinetic effect and that the true thermal $\Delta C_{gas\ ex}$ gradient might be somewhat closer to the potential thermal $\Delta C_{gas\ ex}$ gradient, $\Delta C^{therm,\ pot}_{gas\ ex}$.

We use our second and third thought experiments with an isothermal ocean and fully operational soft-tissue and carbonate pumps to elucidate the influence of biology on air-sea gas exchange (figure 8.4.1). We have seen above that, in the absence of air-sea gas exchange, the interior ocean distribution of *sDIC* would be directly proportional to either phosphate (soft-tissue pump) or potential alkalinity (carbonate pump). If we turn on infinitely rapid air-sea gas exchange, surface waters will become fully equilibrated with a fixed atmosphere of 280 μatm.

In the case of the soft-tissue pump, gas exchange in the high latitudes, where the elevated *sDIC* waters of the deep ocean come to the surface, would cause a loss of CO_2 to the atmosphere, depleting the waters in *sDIC* relative to a case without gas exchange. Conversely, gas exchange in the low latitudes would lead to an uptake of CO_2 from the atmosphere, as the biological fixation of CO_2 creates a deficit of CO_2 relative to the atmosphere. Both changes lead to a reduction of the surface-to-deep gradient. We can estimate the resulting surface-to-deep gradient in *sDIC* from O_2, as the cycling of CO_2 in the rapid gas exchange case would follow very closely that of O_2, except for a small deviation caused by surface variations in *sAlk*. The reason this works is because the surface concentration of O_2 is generally very close to saturation, as expected in a case of infinitely rapid air-sea gas exchange. In particular, in an isothermal ocean with biology and infinitely fast gas exchange, the interior distribution of *sDIC* would be directly proportional to the apparent oxygen utilization (*AOU*), with the proportionality given by the C:O_2 ratio of organic matter remineralization. Thus, multiplying the mean global surface-to-deep *AOU* gradient with $r_{C:O_2} = 117 : -170$ [*Anderson and Sarmiento*, 1994], and subtracting the result from ΔC_{soft}, i.e., the *sDIC* distribution that would exist in the absence of gas exchange, we arrive at a soft-tissue pump contribution to $\Delta C^{bio,\ pot}_{gas\ ex}$ of about -145 μmol kg^{-1}.

In the case of the carbonate pump, turning on infinitely fast gas exchange would lead to an effect opposite to that in the case of the soft-tissue pump. As the high latitudes in such an ocean would have very high concentrations of *sAlk* relative to *sDIC* due to the presence of a dissolution signal from the deep ocean, these waters would tend to take up CO_2 from the atmosphere. The low latitudes, in turn, would tend to lose CO_2 as the excess of $CaCO_3$ formation over dissolution drives oceanic pCO_2 above that of the atmosphere (see figure 8.3.5). Therefore, the presence of air-sea gas exchange enhances the surface-to-deep *sDIC* gradient in a case where the formation and dissolution of $CaCO_3$ is the only biological process. This enhancement can be approximated by calculating the difference between the *sDIC* concentration in equilibrium with the atmosphere for a constant salinity-normalized alkalinity and the *sDIC* equilibrium concentration for the observed preformed alkalinity (taken from *Gruber et al.* [1996]). As it turns out, this enhancement, i.e., the carbonate pump contribution to potential $\Delta C^{bio}_{gas\ ex}$, is almost an order of magnitude smaller than that of the soft-tissue pump, amounting to only about 15 μmol kg^{-1}. Adding the potential carbonate and soft-tissue pump components together, we arrive at a total contribution of $\Delta C^{bio,\ pot}_{gas\ ex}$ of -130 μmol kg^{-1} (figure 8.4.4).

When we use a realistic air-sea gas exchange instead, the gas exchange–induced reduction of the imprint of the biological pumps is smaller (figure 8.4.4). This leads to a vertical *sDIC* gradient from the biological pumps and the $\Delta C^{bio}_{gas\ ex}$ pump that is somewhere between the fully expressed biological pumps (figure

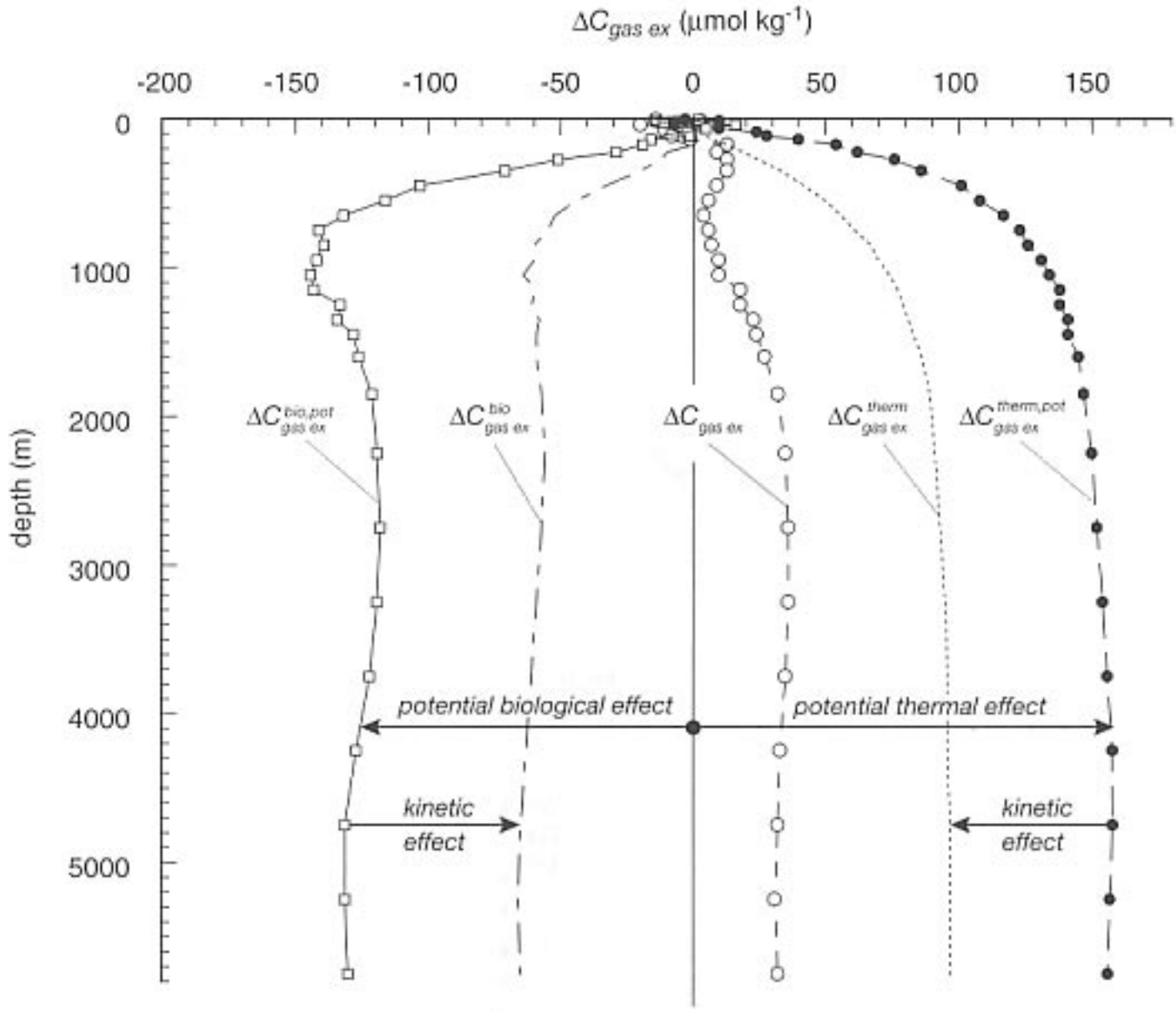

FIGURE 8.4.4: Global mean profiles of the two biological and the two thermal gas exchange pump components. The potential $\Delta C^{therm}_{gas\ ex}$ was calculated assuming that surface *sDIC* is in equilibrium with the atmosphere using a constant salinity-normalized total alkalinity. The potential $\Delta C^{bio}_{gas\ ex}$ was computed from *AOU* taking into account a change in the surface *Alk* concentration due to biology on the basis of preformed surface alkalinity estimates [*Gruber et al.*, 1996]. The kinetic $\Delta C^{therm}_{gas\ ex}$ profile is taken from the model of *Murnane et al.* [1999], and the kinetic $\Delta C^{bio}_{gas\ ex}$ component was calculated by difference.

8.4.1d) and the potential $\Delta C^{bio}_{gas\ ex}$ case (figure 8.4.1e). This means that the kinetic $\Delta C^{bio}_{gas\ ex}$ is positive, i.e., it increases the surface-to-deep gradient in *sDIC* (figure 8.4.4). As was the case for the kinetic $\Delta C^{therm}_{gas\ ex}$ contribution, it is currently not possible to estimate the kinetic $\Delta C^{bio}_{gas\ ex}$ contribution directly from data. However, if we adopt the estimated $\Delta C^{therm}_{gas\ ex}$ of *Murnane et al.* [1999], the kinetic effect on the biological component of $\Delta C_{gas\ ex}$ is substantial and amounts to around 60 µmol kg^{-1}. This results in a $\Delta C^{bio}_{gas\ ex}$ component of only about −70 µmol kg^{-1} (figure 8.4.4).

While the exact values of the kinetic components are not known, the overall conclusion is very clear. The small imprint of air-sea gas exchange on the vertical *sDIC* distribution ($\Delta C_{gas\ ex}$) is a consequence of generally opposing tendencies of $\Delta C^{bio}_{gas\ ex}$ and $\Delta C^{therm}_{gas\ ex}$. The magnitude of these two components depends on the magnitude of biological fluxes and heat fluxes that create "potential" gas exchange fluxes, and the kinetics of air-sea exchange that determines to what degree these two potential pumps are realized. If the simulations by *Murnane et al.* [1999] are approximately correct, it appears that in the present ocean, a relatively small fraction of the potential gas exchange pumps are expressed.

This hypothesis was recently investigated in greater detail and confirmed by *Toggweiler et al.* [2003a, b]. They also highlighted that this kinetic limitation and how it is represented in different ocean models determines to a substantial degree how strongly atmospheric CO_2 responds to changes in upper ocean biology and chemistry, particularly when these changes occur in the high latitudes. We will come back to this topic in chapter 10, as it has strong implications on how we can explain the large atmospheric CO_2 variations associated with glacial-interglacial cycles in climate.

ATLANTIC VERSUS PACIFIC

The high $\Delta C_{gas\ ex}$ concentrations of the deep Atlantic in contrast to the low concentrations in the Pacific can be understood following arguments similar to those used to understand the global mean distribution of $\Delta C_{gas\ ex}$. However, it is this time more instructive to trace the

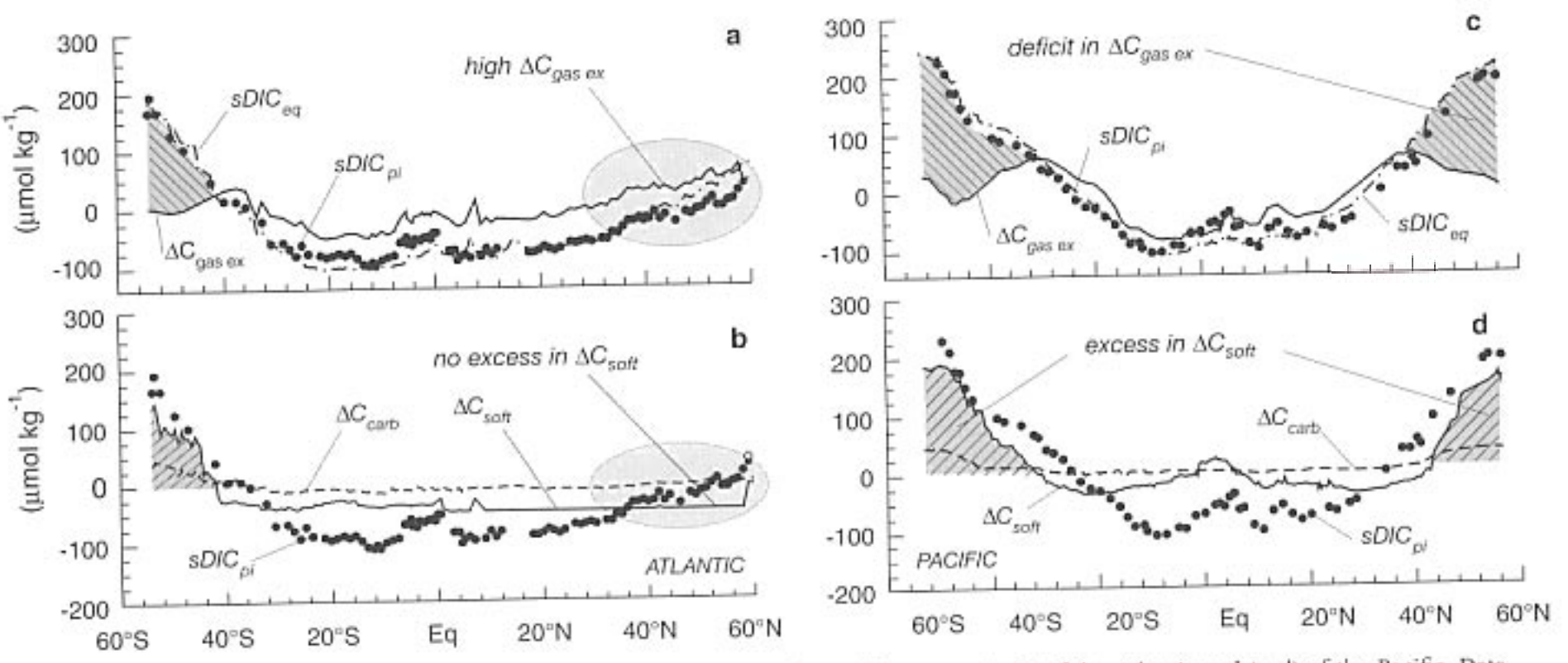

FIGURE 8.4.5: Meridional variations of the ocean carbon pumps in the surface waters (a–b) of the Atlantic and (c–d) of the Pacific. Data are from WOCE cruises A16 and P16.

different water masses back to the places where they were last in contact with the atmosphere and obtained their air-sea gas exchange signal.

The $\Delta C_{gas\ ex}$ signal in the deep Atlantic is associated with NADW, and since this water is formed in the northern North Atlantic, we have to look at surface water properties there. To better understand the particularities of the North Atlantic, it is helpful to contrast this basin with the surface distribution in the Pacific.

Figure 8.4.5 shows surface ocean concentrations of $\Delta C_{gas\ ex}$ as a function of latitude in the Atlantic and Pacific. Also shown are the equilibrium *sDIC* concentrations and reconstructed preindustrial *sDIC* concentrations ($sDIC_{pi}$). We subtracted a global mean surface concentration from the latter two in order to emphasize trends. The first point we note is that $\Delta C_{gas\ ex}$ shows more variations at the sea surface than we have seen in the water column. However, differences in $\Delta C_{gas\ ex}$ between the temperate latitudes, where most of the thermocline waters are formed, and the polar latitudes of the southern hemisphere, where most of intermediate and deep waters of the Indian and Pacific have their sources, are relatively small, e.g., maximally about 50 μmol kg^{-1}. This is consistent with our observation of a very small vertical gradient in $\Delta C_{gas\ ex}$, since the Indian and Pacific dominate the global mean profile.

By contrast to the Pacific, the $\Delta C_{gas\ ex}$ signal in the North Atlantic increases continuously toward the north, reaching higher levels than found in the North Pacific and in the Southern Ocean. While this explains where the signals observed in the interior come from, it does not explain why the different regions have such a different surface expression of $\Delta C_{gas\ ex}$.

If air-sea gas exchange were infinitely fast and there were no biology, $\Delta C_{gas\ ex}$ would follow the equilibrium *sDIC* concentration $sDIC_{eq}$ shown in figure 8.4.5 (note that the equilibrium concentration is equal to $\Delta C_{gas\ ex}^{therm.\ pot}$). In such a case, waters that flow from low latitudes to high latitudes and vice versa would need to exchange large amounts of CO_2 with the atmosphere to account for the large temperature sensitivity of *sDIC*. The $\Delta C_{gas\ ex}$ in the North Atlantic Ocean has the same structure as $sDIC_{eq}$, suggesting that these waters do indeed pick up the required CO_2 from the atmosphere. However, $\Delta C_{gas\ ex}$ in the North Pacific behaves quite differently. It follows the *sDIC* equilibrium concentration south of 40°N, but drops well below the *sDIC* equilibrium trend to the north of this. Despite this failure to take up CO_2 from the atmosphere, the surface water $sDIC_{pi}$ is everywhere very close to $sDIC_{eq}$. Obviously, a process other than uptake of CO_2 from the atmosphere must increase the $sDIC_{pi}$ in the North Pacific. Note that the southern hemisphere high latitude waters also behave the same as the North Pacific.

The solution is revealed in the lower panels of figure 8.4.5, which show the contribution of the two biological pumps to surface ocean *sDIC* variations. It turns out that these pumps provide the necessary mechanism to change surface ocean *sDIC*. The surface waters in the Southern Ocean contain large amounts of *sDIC* that stem from the remineralization of organic matter and the dissolution of $CaCO_3$ (high ΔC_{soft} and ΔC_{carb}). This is a consequence of upwelling processes that bring intermediate and deep ocean waters with high ΔC_{soft} and ΔC_{carb} to the surface, and a biological pump that is relatively inefficient (see chapter 4) and therefore not able to remove these biological signals as rapidly as they are brought up.

When these waters are transported from the Southern Ocean to low latitudes, biological production removes

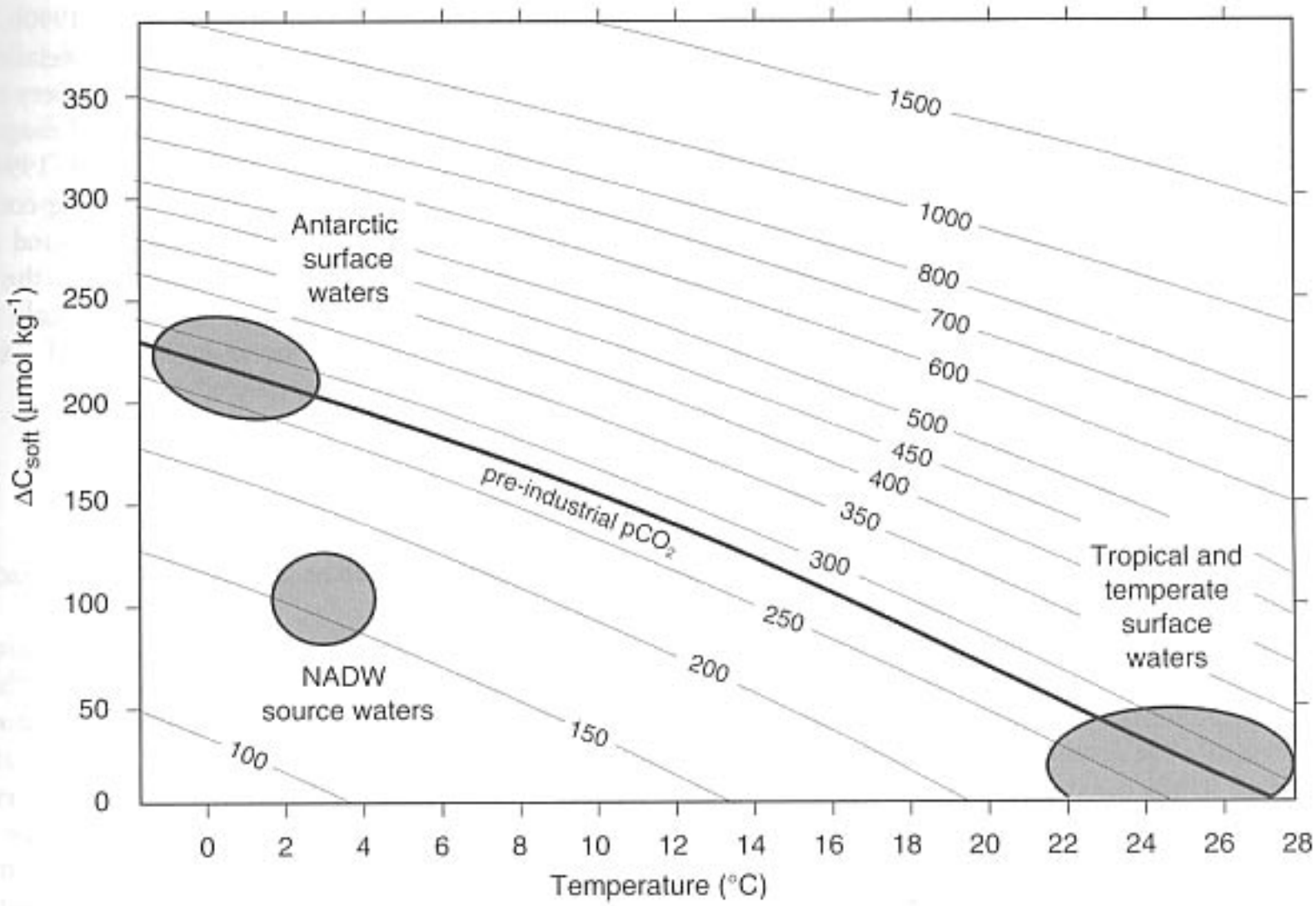

FIGURE 8.4.6: Contours of CO_2 partial pressure (in μatm) for a water sample with salinity of 35, a preindustrial *DIC* concentration of 1900 μmol kg^{-1}, and an alkalinity of 2310 μmol kg^{-1}, as a function of water temperature and phosphate content (and hence also ΔC_{soft} content). The heavy contour is that representing the preindustrial atmosphere (280 μatm). The important point here is that the high content of ΔC_{soft} compensates for the low temperature of Antarctic surface waters, giving them nearly the same pCO_2 as warm nutrient-free surface water. By contrast, because of their lower ΔC_{soft} content, surface waters in the northern Atlantic take up CO_2 given off to the atmosphere by other regions of the ocean. Adapted from *Broecker and Peng* [1992].

almost all of this "excess" ΔC_{soft} and ΔC_{carb}, reducing *sDIC* accordingly. This reduction is apparently of very similar magnitude to the change in *sDIC* required to accommodate the temperature change. Therefore, these waters have to exchange only limited amounts of CO_2 with the atmosphere to remain near equilibrium with the atmosphere.

In the North Atlantic, the contributions of ΔC_{soft} and ΔC_{carb} to surface *sDIC* variations are much smaller, indicating a lesser degree of biological compensation for the thermally driven CO_2 fluxes. This creates a strong tendency for the North Atlantic to take up CO_2 from the atmosphere. Figure 8.4.6 illustrates this difference between surface waters of the North Atlantic and Southern Ocean more explicitly by plotting the ΔC_{soft} for typical surface waters as a function of temperature. Also shown are isolines of calculated pCO_2 assuming a constant alkalinity and a fixed background *DIC* to which ΔC_{soft} was added according to the value given on the ordinate. Although North Atlantic surface waters are warmer than Antarctic surface waters, the much lower ΔC_{soft} concentration of the North Atlantic surface waters leads to their having much lower pCO_2 than that computed for Antarctic surface waters. This gives the North Atlantic surface waters a large potential to take up CO_2 from the atmosphere. By contrast, the Antarctic surface waters are near preindustrial pCO_2, as are typical tropical and temperate surface waters. These waters, therefore, have to exchange little CO_2 with the atmosphere as they are converted from one to another.

The reason for this different behavior of the North Atlantic is the global-scale meridional overturning circulation, which feeds low-nutrient surface waters from the subtropics into the NADW formation region. On the way, these waters are giving off large amounts of heat, leading to a strong cooling [*Schmitz*, 1996]. These waters remain near the surface for a sufficiently long time, so that the slow kinetics of air-sea gas exchange does not impede the uptake of substantial amounts of CO_2 from the atmosphere. This uptake from the atmosphere can occur because the cooling occurs without excessive entrainment of nutrients from below and with it respired CO_2 as is happening in the Southern Ocean. The lack of nutrient entrainment in the North

Atlantic is because the nutrient content of the thermocline is relatively low as a result of the nutrient export by NADW.

An additional factor contributing to the low ΔC_{soft} and ΔC_{carb} signals in the North Atlantic in comparison with the Southern Ocean may be the large difference in the bio-availability of iron. In the Southern Ocean, observational evidence is steadily increasing that the low availability of iron as a result of low atmospheric deposition is preventing the complete drawdown of nutrients, thus creating the largest high-nutrient, low-chlorophyll (HNLC) region [*Martin et al.*, 1990b, 1991; *de Baar et al.*, 1995; *Boyd et al.*, 2000] (see detailed discussion in chapter 4). The atmospheric delivery of iron to the North Atlantic is almost an order of magnitude higher [*Duce et al.*, 1991, *Tegen and Fung*, 1994] and appears to be sufficient to allow the near-complete drawdown of nutrients, creating low ΔC_{soft} and ΔC_{carb} concentration. This example illustrates how the interaction of biological processes with large-scale ocean circulation and possibly the biogeochemical cycles of iron can lead to quite unexpected results.

8.5 Carbon Pumps and Surface Fluxes

In this last section, we would like to close the great biogeochemical loop, and investigate the connection between the ocean carbon pumps and air-sea fluxes of CO_2. In particular, we will look at the biological and thermal components of the gas exchange pump, in order to understand what drives the CO_2 fluxes across the air-sea interface. Unfortunately, it is not possible to split the observed air-sea flux of CO_2 into these two components. We therefore use model results as an illustration.

Following *Murnane et al.* [1999], we ran two parallel simulations in an ocean biogeochemistry model, one with the thermal gas exchange pump only, and a second one that includes both biological pumps. The latter simulation is termed "combined pump." The difference in air-sea CO_2 fluxes between these two simulations is taken as the contribution of the biological gas exchange pump. The model employed here is very similar to that described in detail in chapter 5 except that a representation of the carbonate pump has been included as well. In order to arrive at a realistic atmosphere-ocean distribution of CO_2, all simulations were run to a quasi steady-state by setting atmospheric CO_2 to its pre-industrial value of 280 ppm and letting the ocean adjust to this concentration (see *Najjar and Orr* [1998] for details). This takes several thousand years of spin-up.

Figure 8.5.1a shows the meridional pattern of the zonally integrated air-sea gas exchange as predicted by this model. The patterns exhibited by the thermal gas exchange pump are related to the transport of heat and water within the ocean and its exchange with the atmosphere. In the high latitudes, surface waters lose heat to the atmosphere and consequently take up CO_2 from the atmosphere. In the equatorial regions, colder waters that are upwelled to the surface are warmed up, which leads to a loss of CO_2 to the atmosphere. The correlation of the air-sea exchange fluxes of CO_2 with the heat fluxes are modified, however, by the slow air-sea exchange of CO_2 relative to heat. This shows up particularly in the equatorial region, where the peak of the CO_2 gas exchange is much wider than would be predicted by the heat exchange alone.

The biological pump represents, to a first approximation, a closed loop within the ocean. Waters that are brought to the surface contain an excess of inorganic carbon stemming from the biological pump relative to these surface waters. At the same time, these waters also contain an excess of nutrients. Biological uptake at the surface is generally fast enough to strip out all or most of the nutrients and the excess CO_2 before CO_2 is lost to the atmosphere. Only in regions where the biological uptake is inefficient in reducing the nutrients and the associated biological inorganic carbon coming to the surface will CO_2 escape into the atmosphere. As we discussed in detail in chapter 4, a good diagnostic of such regions of low efficiency is high surface-nutrient concentrations, which occur in the Southern Ocean, in the equatorial Pacific, and in the North Pacific. The Southern Ocean, characterized by the highest surface ocean-nutrient concentration, also represents the region with the highest loss of CO_2 to the atmosphere associated with the biological pump. This biologically induced outgassing outweighs the uptake of CO_2 from the atmosphere as a consequence of the thermal gas exchange pump, leading to a small residual outgassing in the combined pump scenario in this region (figure 8.5.1a). This is exactly the same compensation that we alluded to before when trying to explain the low vertical $\Delta C_{gas\ ex}$ signal in the observations. The loss of CO_2 in the high latitudes due to the biological pump is compensated by a net uptake of CO_2 in the mid-latitudes, so that the global net exchange of CO_2 in association with the biological pump is zero as required. Simulations of the contribution of the carbonate pump to the variation in the biological pump show it to be generally small [*Murnane et al.*, 1999].

The pattern of the zonally integrated air-sea exchange due to the combined pumps represents the sum of the patterns generated by the thermal and biological pumps. In this particular model, the thermally forced CO_2 fluxes tend to dominate, except in the Southern Ocean. The air-

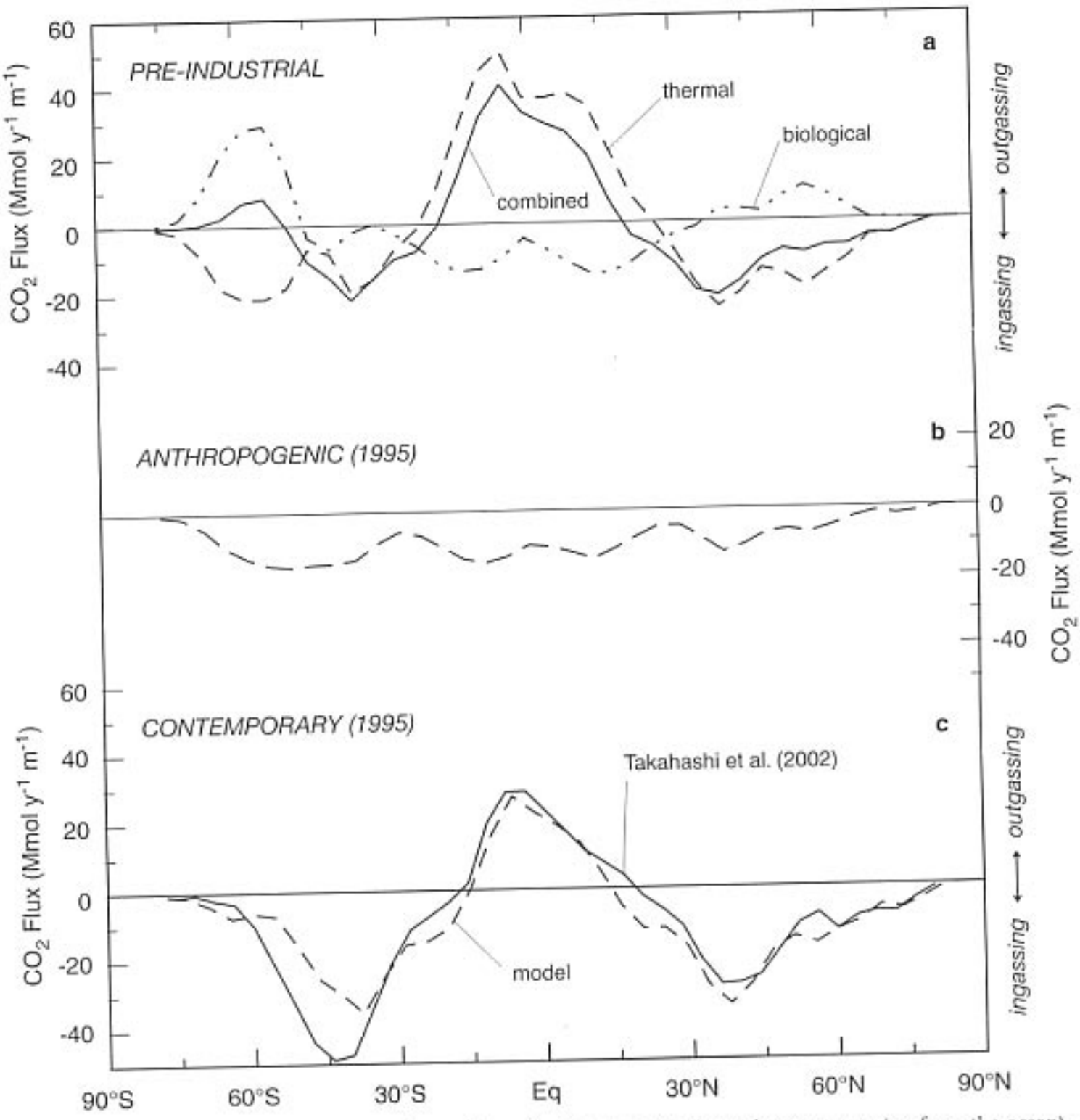

FIGURE 8.5.1: Zonally integrated sea-air exchange fluxes for CO_2 (positive fluxes denote outgassing from the ocean). (a) Model-simulated sea-air fluxes of CO_2 induced by the thermal gas exchange pump, the biological gas exchange pump, and the sum of these two pumps. (b) Model-simulated sea-air flux of anthropogenic CO_2 for 1995. (c) Model-simulated total sea-air flux for 1995 in comparison to observationally derived fluxes based on the ΔpCO_2 climatology of *Takahashi et al.* [2002] as estimated by *Wanninkhof et al.* [2002]. The model employed is the KVLOW-AILOW model as described by *Gnanadesikan et al.* [2002].

sea CO_2 fluxes induced by the two gas exchange pumps generally tend to oppose each other, similar to what we have seen for their influence on the ocean interior distribution of *sDIC* in section 8.4 above.

Our model-based conclusions about the relative roles of the two driving forces for the exchange of CO_2 across the air-sea interface would be strengthened if we could demonstrate that the model with the combined pumps compares well with observationally based flux estimates. The latter can be obtained by combining the observed air-sea pCO_2 difference (see figure 8.1.1) with an estimate of the gas exchange coefficient (see chapter 3). Before we can undertake this comparison, we have to take into account that the anthropogenically driven increase of atmospheric CO_2 has led to a substantial perturbation of the air-sea CO_2 fluxes, which cannot be separated from the observed fluxes. However, it is relatively straightforward to simulate these anthropogenic CO_2 perturbation fluxes (see chapter 10 below) in our model, as this simply requires the model to be run further forward in time, while changing the atmospheric CO_2 concentration according to its observed time history. Figure 8.5.1b shows that the anthropogenic perturbation flux is directed into the ocean everywhere, with largest magnitude in the regions where intermediate and deep waters come to the surface, i.e., in the tropics, along upwelling margins, and in mid- and high-latitude regions with intense convection.

If we add this anthropogenic perturbation flux to the CO_2 fluxes from the combined pump simulation, the resulting total flux compares reasonably well with the observationally based estimates (figure 8.5.1c). This suggests that the model is fundamentally able to represent the biological and thermally driven components. We therefore conclude that our model-based result of generally competing effects on air-sea fluxes of CO_2 arising from thermal and biological forcing applies also to the real world. This conclusion has major implications for how the ocean responds to changes in climate, as any change in meteorological forcing impacts both the thermal and biological components of air-sea gas exchange. We will show in chapter 10, for example, that future climate change will lead to a substantial thermally forced reduction in the uptake of anthropogenic CO_2 from the atmosphere. Climate-induced changes in the biological forcing, however, will lead to an enhancement of this uptake, albeit of smaller absolute magnitude than the thermally forced reduction, causing the total uptake to lie in between the thermally and biologically forced solutions. The exact magnitude of these climate change–induced changes in the uptake of anthropogenic CO_2 from the atmosphere is currently poorly understood and represents a major research issue.